Rock Mechanics and Rock Engineering (2025) 58:4043–4067
https://doi.org/10.1007/s00603-024-04347-x

ORIGINAL PAPER

Unveiling Axial Load Transfer Mechanism in Fully Encapsulated Rock Bolts

Hadi Nourizadeh[1,2] · Ali Mirzaghorbanali[1,2] · Kevin McDougall[3] · Hani Mitri[4] · Peter Craig[5] · Ashakan Rastegarmanesh[1] · Naj Aziz[6]

Received: 11 September 2023 / Accepted: 16 December 2024 / Published online: 11 January 2025

Abstract

Determining the axial load transfer mechanism of rock bolts under various conditions is paramount for ensuring efficient reinforcement in rock structures, advancing our understanding of rock support and ability to design robust engineering solutions. This paper presents the results of an experimental study aimed at investigating the factors affecting axial load transfer mechanisms in fully encapsulated rock bolts including embedment length, mechanical characteristics of bonding materials, and host rock conditions. The results show that increasing the embedment length improves the pullout capacity, but only up to a critical length, beyond which the ultimate strength and bond stress distribution remain constant. Amongst the mechanical characteristics, shear modulus of the bonding materials was found the most significant factor influencing axial load transfer and the bond stress distribution. Compressive strength of bonding materials, which is commonly used to assess performance, should not be the only factor considered, as shear properties were found more representative. The expansion characteristics of the bonding agents were also found to be effective in improving pullout performance. The study also provides a detailed explanation of how the mechanical properties of host rocks affect the pullout capacity of bolts. Specifically, it states that greater stiffness result in higher pullout strength.

Highlights

- Shear modulus of the bonding materials impacts the bond stress distribution.
- The effect of radial stiffness on rock bolts' axial performance was studied.
- The effect of grout and rock on the performance of rock bolts was examined.
- The distribution of bond stress along the encapsulation length was analyzed.
- The failure pattern of fully grouted rock bolts was examined.

Keywords Rock bolts · Bonding materials · Pullout tests · Bond stress distribution · Anchoring grouts and resins

✉ Hadi Nourizadeh
hadi.nourizadeh@unisq.edu.au

[1] Centre for Future Materials (CFM), University of Southern Queensland, Toowoomba, QLD 4350, Australia

[2] School of Engineering, University of Southern Queensland, Springfield Central, QLD 4300, Australia

[3] School of Surveying and Built Environment, University of Southern Queensland, Toowoomba, QLD 4350, Australia

[4] Department of Mining and Materials Engineering, McGill University, Montreal H3A 0E8, Canada

[5] Jennmar Australia Pty Ltd, Sydney, NSW, Australia

[6] School of Civil, Mining and Environmental Engineering, University of Wollongong, Wollongong, NSW 2500, Australia

1 Introduction

Rock reinforcement is a common approach used in tunnels, underground structures, underground excavations to stabilize and enhance the capacity of the rock mass (Rastegarmanesh et al. 2022, 2023). This method comprises a wide range of materials and techniques, among which rock bolting is one of the most effective and economical (Grasselli 2005). Rock bolts vary in terms of design and material, but the fully grouted rock bolt is the most widely used in practice (Høien et al. 2021; Nourizadeh et al. 2021). Once a rock bolt is installed in a borehole and grouted, it interacts with the grouting materials and the surrounding rock mass as soon as deformations occur in the rock mass. Due to displacements in the rock mass, the load is transferred from the unstable rock to the grouting materials and then to the bolt and subsequently to the intact rocks. This complex interaction restrains rock movement along a discontinuity and controls rock deformation along the grouted length. When a grouted bolt is subjected to a tensile force, the induced axial stress in the rod is distributed across the bolt-grout interface, the grout, the grout-rock interface, and the rock. The load is transferred and redistributed between the bolt and the host rock by bond (shear) resistance in the grout resulting from adhesion and mechanical interlocking between the bolt-grout and the grout-rock (Signer 1990). The overall behavior and capacity of encapsulated rock bolts are influenced by several factors, including confining stresses, bolt surface profile, grout mechanical properties, and the surrounding rock mass conditions. Nourizadeh et al. (2023b) demonstrated that increasing confining stress enhances the ultimate bearing capacity of the bolt. However, they noted that true in-situ stress conditions, which involve triaxial states, may impact bolt performance differently compared to the biaxial conditions typically assumed in hydrostatic testing. The uneven surfaces of the bolt and drill hole provide irregular contacts at the bolt-grout and grout-rock interfaces. When the bolt is subjected to a load, stress concentration occurs at these asperities and irregularities, and the bond strength comes into play in the form of interlocking. Various types of failure can occur in response to axial bolt loads, and the type, magnitude, and direction of the distributed stress, along with the material properties of the components, dictate the main failure mode of the system. Wu et al. (2024) conducted static tests on L- and J-shaped anchor bolts to examine the effects of various parameters. The results indicated that the uplift bearing capacity of L- and J-shaped anchor bolts was significantly higher than that of smooth bolts. The encapsulation length basically determines whether a failure occurs in the bolt or in another component. If the encapsulation length is sufficient to transfer all the load, then the bolt itself will fail once the applied load exceeds the ultimate capacity of the bolt. Alternatively, if the encapsulation length is insufficient, then localized failure takes place where the induced stresses exceed the material strength (either grout or rock). In the cross-sectional view, analytical solutions indicate that the induced bond stress is maximum at the bolt-grout interface and decreases exponentially with distance from the interface (Tepfers 1979). Therefore, it is reasonable to assume that if the surrounding rock is relatively strong and bonding at the grout-rock interface is sufficient to withstand localized stresses, then failure occurs at the bolt-grout interface. However, other critical properties of the rock, such as its formation, lithology, and structural features, should also be considered as key factors that must be taken into account (Benge et al. 2021; Katende 2022; Katende et al. 2021, 2022, 2023). Failure at the bolt-grout interface has been often reported as the main failure in the literature, although fractures, partial failure, and deformation in other parts have been observed to occur simultaneously. Sun et al. (2024) innovatively engineered an intelligent terminal structure aimed at modifying the behavior of rock bolts. When debonding at the bolt-grout interface occurs, the deformation of the other parts can usually be neglected (Antino et al. 2016). In this case, the axial behavior of the rock bolt can be effectively studied by examining the stress distribution along the bolt-grout interface. Pullout tests are frequently employed to assess the axial behavior and anchorage capacity of grouted rock bolts. However, non-destructive testing techniques are also utilized for the same purpose (Wu et al. 2019). Studies have shown that the evolution of stresses along the encapsulation length is non-uniform, and that the stresses decrease with distance from the loading point. Initially, the peak bond stress is captured near the loading end, but it decreases once debonding occurs and shifts incrementally towards the free end Farmer (1975) investigated the axial behavior of fully grouted rock bolts and developed a theoretical model showing that the bond stress attenuates exponentially from the loading point to the far end of the bolt. The proposed theory was comparable to experimental results at lower anchor loads. Li and Stillborg (2000) introduced a bond model for fully grouted rock bolts that illustrates how the bond stress develops from the loading end to the free end. The proposed model consists of four main parts, including a fully decoupled part where the bond stress is zero, a partially decoupled part with constant residual bond strength, a linear softening part which reaches the peak strength, and finally a compatible deformation part where the bond stress decreases exponentially towards the free end of the bolt. The latter stage can be matched with the elastic stage introduced in other models. Benmokrane et al. (1995) assumed an average distribution of bond stress along the anchored length and expressed a trilinear debonding model between the induced bond stress and global slip based on experimental investigations. Afterwards, numerous trilinear bond-slip models were proposed,

including those by Li et al. (2021), Martín et al. (2011), Cai et al. (2004), He et al. (2015) Ren et al. (2010), Chen et al. (2020), Ma et al. (2013), Chen and Li (2022) and Zhou et al. (2010). Instrumented rock bolts using electric sensors, such as resistive strain gauges and fiber optics, have also been effectively used to measure axial strain along the anchored length to estimate the load. This information can be used to quantify the induced bond stress along the encapsulation length (Chen et al. 2020; Farmer 1975; Freeman 1978; Huang et al. 2013; Singer et al. 1997; Teymen and Kılıç 2018; Vlachopoulos et al. 2018; Zhang et al. 2006). Several factors, including rock bolt geometry, bolt surface configuration, mechanical characteristics of the bolt, grout, and host rock, boundary conditions, anchorage length, drilling quality and drillhole diameter, annulus thickness, and installation and grouting quality affect the axial behavior and bearing capacity of grouted bolts (Chen and Xiao 2024). Some of these factors can be engineered to improve the system's performance (Aziz et al. 2016). Thus, a proper understanding of the combined effects of these factors is essential for practical rock bolting design.

Figure 1 illustrates the possible load-slip relationships in the pull-out process of grouted rock bolts. At the critical encapsulation length, the anchorage strength of the unit exceeds the yield strength of the bolt. If the encapsulation length is much longer than the critical encapsulation length, the bolt failure occurs in the shank (Wee et al. 2016) (curve A in Fig. 1). If the encapsulation length is slightly over the critical encapsulation length bolt debonding occurs, however, bolt undergoes a plastic deformation (curves B and C in Fig. 1). If the encapsulation is shorter than the critical encapsulation length, debonding of the bolt will occur before reaching the peak capacity (curve D in Fig. 1). Ren et al. (2010) proposed a closed-form analytical solution for bolts with a critical encapsulation length showing snapback form (curve C in Fig. 1). This model includes five stages: elastic stage (1), elastic-softening stage (2), elastic-softening-debonding stage (3), softening-debonding stage (4), and debonding stage (5). The model exhibits a snapback form of the load-slip relation, although the authors could not capture the snapback phenomenon in the experimental tests. The absence of sufficient radial stiffness may lead to splitting failure (curve E in Fig. 1).

Rock mass conditions play a vital role in the failure mode of rock bolting systems. The high quality of the host rock not only assures that the failure will not occur in the rock, but it may also enhance the performance of the system (Benge et al. 2023; Moosavi et al. 2005). The axial slip of deformed bars generates radial dilation, which is inhibited or restricted by the normal stiffness of the rock mass. Hyett et al. (1992) indicate that in higher radial stiffness, dilation is suppressed, and shear-off failure occurs at the bolt-grout contact, leading to greater load-bearing capacity, whereas in lower radial stiffness, the propagation of radial cracks through the grout annulus is predictable, resulting in a decrease in radial stress at the bolt-grout interface and thus an instantaneous reduction in the bond resistance to pull-out. Yilmaz et al. (2013) conducted pullout tests on chemical anchors embedded in weak concrete, indicating the positive contribution of the concrete strength to the bond strength. On the contrary, Cao et al. (2014) reported the insignificance of the host rock uniaxial compressive strength (UCS) ranging from 30 to 136 MPa on the pullout capacity of rock bolts.

It has been shown that the mechanical properties of the bonding agent have a significant impact on the response of rock bolts. For example, Yokota et al. (2019) found that the interfacial shear stiffness is slightly lower for specimens prepared with low-strength mortar. Teymen and Kılıç (2018)

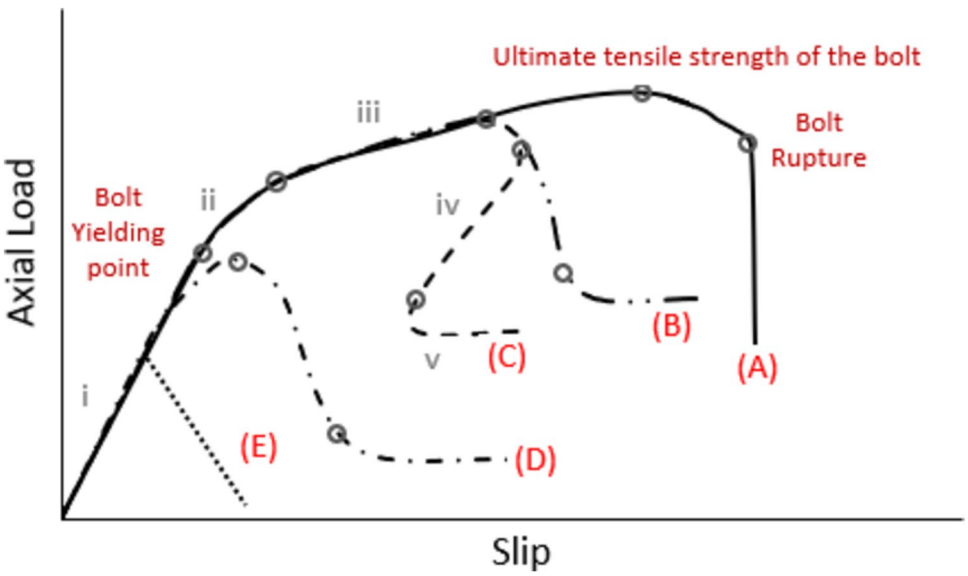

Fig. 1 Potential load-slip relations for fully grouted rock bolts (adopted from Li et al. 2016; Ren et al. 2010; Zou et al. 2020))

concluded that the bond strength of fully grouted rock bolts increases logarithmically with an increase in the shear strength of the grout. However, in the experimental studies conducted by Benmokrane et al. (2000) and McKay and Erki (1993), a clear relation between grout strength and anchor performance was not observed. Benmokrane et al. (1995) indicated that an increase in the modulus of elasticity of grouts can result in higher radial stiffness at the bolt-grout interface and, therefore, improve bond strength. Małkowski et al. (2022) found the importance of the curing time on the pullout performance of rock bolts specifically for the cementitious grout. The influence of curing on resin-based encapsulation materials exhibits limited efficacy beyond the initial 48-h window. Conversely, cementitious grouts demonstrate a substantial enhancement in their performance following this designated timeframe. Nourizadeh et al. (2023a, b) found that the shear properties of the bonding agent are the primary factor that significantly impacts the performance of fully encapsulated rock bolts. Katende et al. (2020) found that contaminations affect the mechanical properties of the cementitious grouts.

The literature includes many experimental, numerical, and mathematical studies on the axial behavior of rock bolts, however, there is a need to comprehensively analyze the performance of fully grouted rock bolts under different geotechnical conditions. This study presents a comprehensive laboratory study on the pullout performance of fully grouted rock bolts and aims to address the four fundamental questions regarding the axial load transfer mechanism of rock bolting. They are (1) What is the effect of embedment length on the distribution of bond stress and failure of the system? (2) What is the effect of bonding material type on the bond stress distribution? (3) What is the relation between peak bond resistance and bonding material type? and (4) What is the effect of host rock properties on the bond stress distribution and failure mechanism of the bolts? The results should provide useful insights for the design and selection of rock bolts for various engineering applications. This information can also effectively contribute to assessing and improving the available analytical solutions for rock bolting design. Three types of chemical agents as well as three types of cementitious grouts with and without additives were used to investigate their mechanical characteristics and influence on the axial behavior of rock bolts. To determine the effect of surrounding rock mass, three different strengths of concrete ranging from 20 to 60 MPa were used. Pullout tests were performed on fully instrumented and encapsulated rock bolts installed in prepared concrete cylinders with varying encapsulation lengths. The purpose of the pullout experiments is to evaluate the combined effect of grout properties, surrounding rock quality, and embedment length on bond behavior. The evolution of the interfacial bond stress along the encapsulation length was also determined by measuring and recording strain values on the mounted strain gauges. Section 2 presents an overview of the materials employed, including their mechanical characteristics. Section 3 delves into the detailed results and analysis of the pullout tests. Lastly, Sect. 4 succinctly outlines the main findings, providing a concise summary.

2 Experimental Campaign

To perform a thorough evaluation of the axial behavior of rock bolts across various geotechnical conditions and applications, a selection of materials was made. These materials encompassed concrete as the surrounding medium, along with encapsulation agents exhibiting diverse applications and mechanical characteristics. This approach ensured a comprehensive understanding of the performance and efficacy of rock bolts in different scenarios. The chosen materials were carefully considered to ensure accurate and reliable assessments.

2.1 Materials

Firstly, steel rock bolts were equipped with resistive strain gauges along the bolt. The rock bolt is first inserted in a hole that is created in the center of the concrete cylinder. The hole is then filled with one of five different types of bonding agents according to the experimental plan. Concrete batches were prepared with three different mix designs to achieve the desired properties.

2.1.1 Surrounding Media

Three concrete mixtures were specifically formulated and designed to achieve M20, M40, and M60 strength grades, following the guidelines of AS-1379. These concrete batches were cast into steel pipes (AS/AZS 1163) with an outer diameter of Ø165.1 mm and a wall thickness of 5.4 mm, simulating rock mass formations ranging from relatively soft to hard strengths. The radial stiffness of the pipe used in this study is sufficient to simulate the infinity and stiffness of the desired surrounding rocks (Cao et al. 2016). It is recommended to use thicker walls as the strength of the concrete increases, however, in this study, we aimed to purely evaluate the effect of concrete strength itself, so using steel tubes with different geometry was deemed unnecessary. Table 1 presents the composition of the concrete mix designs used.

Cylindrical samples were prepared to assess the mechanical properties of the concrete. The specimens were created and cured following ASTM C192, ASTM C39, and ASTM C469. Two sets of perpendicular resistive strain gauges, each measuring 30 mm, were affixed to the midpoints of two diametrically opposite sides of the cylindrical samples (200 mm

Table 1 Summary of concrete mixtures used in the experimental program

Batch	Portland cement[a] (kg)	Aggregate[b] (kg)	Sand (kg)	Flyash (kg)	GGBS[c] (kg)	Silica Fumes (kg)	Superplasticizer[d] (ml)	Shrinkage Reducing agent[e] (ml)	Water (l)	W/binder (%)
M20	261	1081	809	0	65	0	0	1000	168	51.4
M40	323	1183	597	138	0	0	4584	4250	168	36.4
M60	472	987	654	87.3	0	24.3	11,647	10,500	168	28.7

Numbers are for 1 m^3 of wet concrete

[a]General Purpose Portland cement

[b]Nominal maximum size of the aggregate is 10 mm

[c]Grand Granulate Blast-Furnace Slag

[d]Sika® ViscoCrete 10

[e]Sika® Control Plus

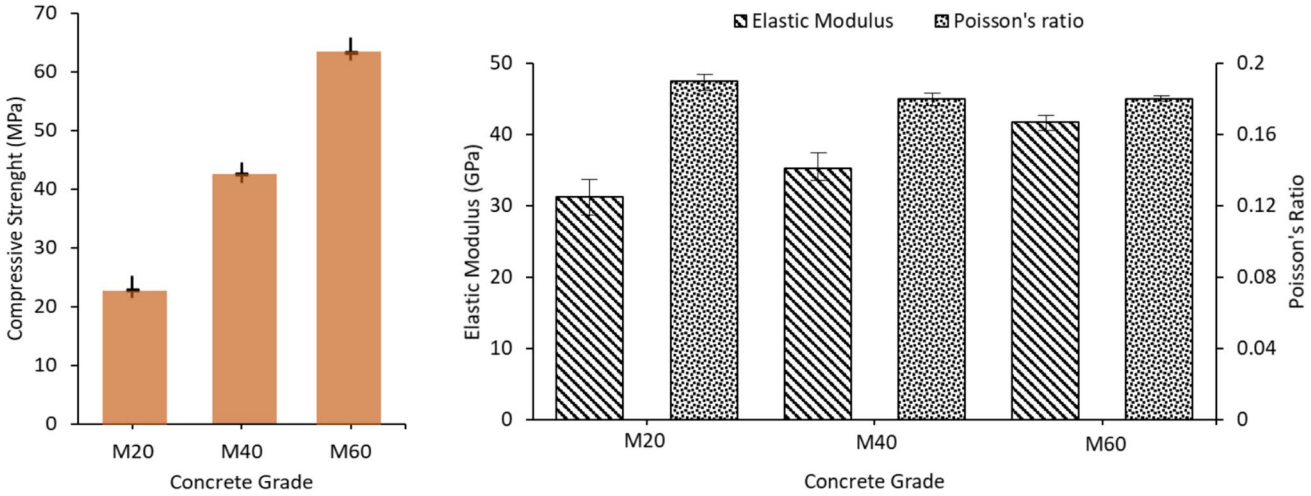

Fig. 2 Compressive strength, elastic modulus and Poisson's ratios of the concrete used as host medium

height × 100 mm diameter) to determine the modulus of elasticity and Poisson's ratio. Figure 2 displays the mechanical characteristics of the various concrete grades used. The average compressive strength of the concrete was measured at 22.8, 42.5, and 63.3 MPa, indicating weak, medium, and hard rock classifications, respectively. The elastic modulus of the specimens ranged from 31.2 to 41.7 GPa, which correlated with the compressive strength. However, no distinct relationship was observed between Poisson's ratio and the other properties. Concrete cylinders were cast in five different lengths: 100, 150, 200, 300, and 400 mm, corresponding to the encapsulation lengths of the bolts. Before casting the concrete, a 28 mm PVC tube was centrally positioned in the mold using specially designed 3D-printed caps to create a hole. Additionally, a flexible polyvinyl tube with a 4 mm diameter was wrapped around the central PVC tube to form a rifled borehole, simulating field drilling conditions (Fig. 3). To ensure a uniform interfacial shear stress throughout the encapsulation length, the rifling was designed with a pitch of zero.

2.1.2 Bonding Materials

Five types of bonding agents were used in this study to encapsulate the rock bolts, consisting of two cement-based grouts, hereafter referred to as G1 and G2, and three types of two-component polyester resins, hereafter referred to as R1, R2, and R3. The aim was to comprehensively reveal the effectiveness of bonding materials with a wide range of properties. G1 is a plain grout with a water-grout (w/g) ratio of 0.25, while G2 is an expansive grout made by adding 1% of an expanding agent, Sika® Quellmittel 1, to G1 grout in the laboratory with a w/g ratio of 0.25. R1, R2, and R3 are specifically synthesized for rock bolting and are based on polyester-based resins diluted with styrene monomer and filled with $CaCO_3$ as the insert fillers. Resins R1 and R2

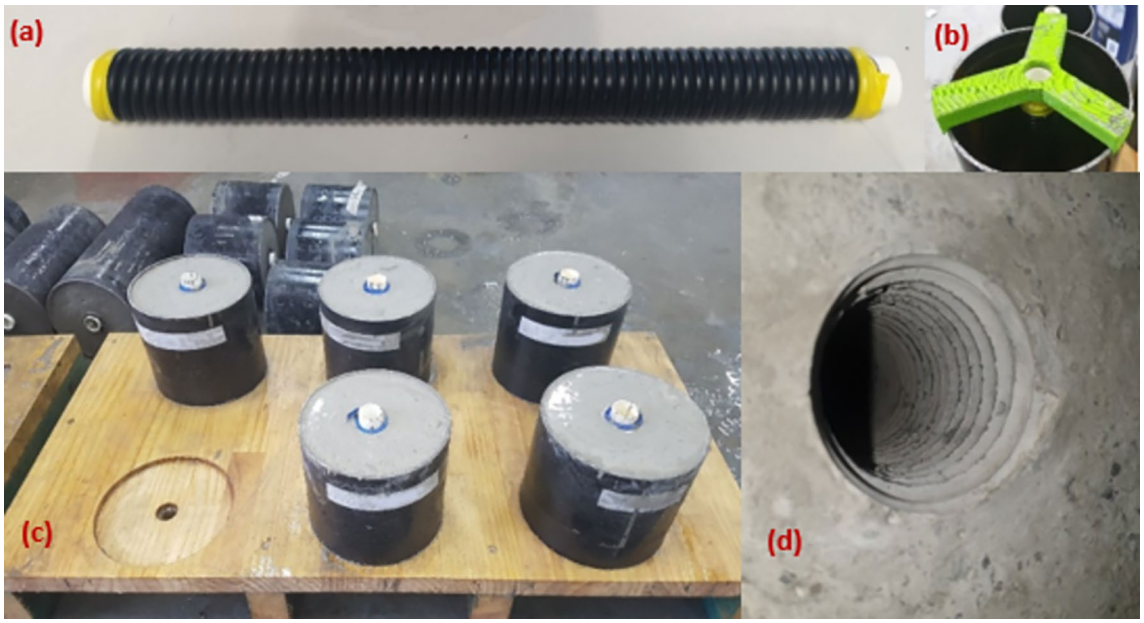

Fig. 3 Concrete casting and rifling the holes; **a** revolving flexible tube around the central PVC pipe for rifling purposes, **b** 3D printed cap for centralizing the central pipe, **c** concrete casting in the steel pipes with the central hole, and **d** rifled holes obtained after concrete curing

Table 2 Summary of the mechanical tests performed on the bonding materials

Test	Standard	Specimen geometry
Compressive	ASTM C579 & ASTM C109	Cubic
Tensile	ASTM D638 & ASTM C307	Dog-Bone
Shear	ASTM D5379	V-notched[a] and Cylindrical[b]

[a]Resin specimens

[b]Grout specimens

were catalyzed using an oil-based catalyst (C1) at a concentration of 8% weight per weight of the total product (%w/w). On the other hand, R3 was activated using a water-based catalyst (C2) at a ratio of 20% w/w. Both catalysts contain the same $CaCO_3$ fillers, but the proportion of benzoyl peroxide is different.

Mixing of the grouts and resins was performed using a laboratory scale mixer according to the recommended mixing time and mixing speed by the supplier in a temperature-controlled system set to 20 °C. Immediately after mixing, the bonding material was pumped into the concrete holes for encapsulation. It was also used to make molds for the determination of the mechanical characteristics. Compressive strength tests were instrumented using resistive strain gauges to measure the lateral and axial strains and consequently calculate the elastic modulus and Poisson's ratio. Table 2 presents a summary of the mechanical tests conducted on the bonding materials used. Figure 4 depicts the results of mechanical tests of the bonding materials applied in this study. The results indicate that the highest magnitudes of compressive strength were recorded by R1 and R2 at 102.5 and 96.4 MPa, respectively. Among the cementitious grouts, G1 is the strongest in compression, standing at 86.6 MPa. The lowest compressive strength was found to be 50.6 and 46.9 MPa for R3 and G2, respectively. Although the resins exhibited better compressive strength, cementitious grouts G1 and G2 showed stiffer behavior in compression, resulting in a higher elastic modulus, which was measured at 27.2 and 20.1 GPa, respectively. The elastic modulus of the resins, R1, R2, and R3, was found to be much less compared to the cementitious grouts at 8.03, 7.45, and 4.71 GPa, respectively. Similarly, the resins represented higher relative deformation in the direction perpendicular to loading, leading to higher Poisson's ratios than grout. The Poisson's ratio was found to be 0.16, 0.18, 0.48, 0.47, and 0.43 for G1, G2, R1, R2, and R3, respectively.

2.1.3 Rock Bolt and Instrumentation

Deformed steel M24 X Coal Bolts, manufactured by Minova Australia, were used as rock bolts in the tests, with varying lengths. Coal Bolts are often used in Australia for rock support and have a core diameter of 22 mm and a nominal total (rib to rib) diameter of 24 mm. Table 3 lists the geometrical

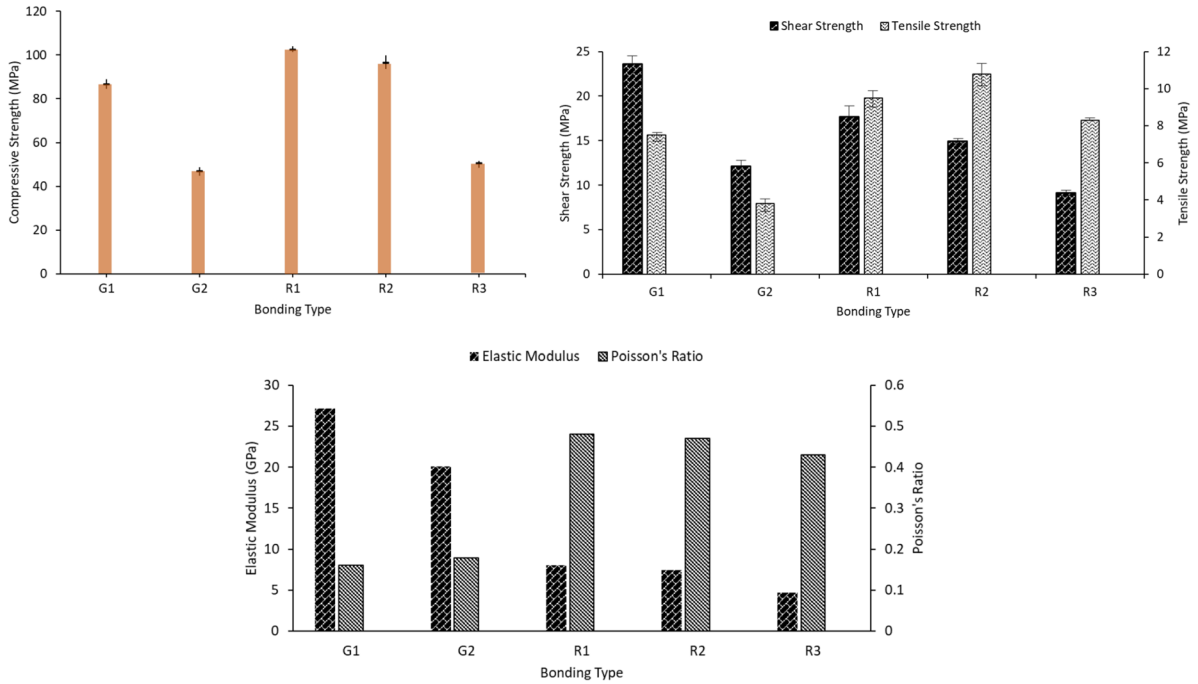

Fig. 4 Mechanical characteristics of the bonding materials

Table 3 Physical and mechanical properties of the original rebar bolt

Elastic modulus (GPA)	Nominal cross-section area (mm^2)	Core diameter (mm)	Nominal Bolt diameter (mm)	Nominal yield load (kN)	Nominal tensile capacity (kN)	A_{gt} [a] (%)
210	370	22	24	220	310	8

[a] A_{gt} is the total elongation at maximum force

and mechanical characteristics of the Coal Bolts. The rock bolts were modified with a pair of opposed, right-angle U-shaped grooves (4 × 4 mm) for instrumentation purposes. These grooves were machined diametrically along the longitudinal ribs of the rock bolts. Axial deformation was monitored by mounting resistive strain gauges along the embedment length. This method has been successful in monitoring the axial deformation of rock bolts in previous technical developments (Signer 1990). The resistive strain gauges were 3 mm in length with a nominal gauge resistance of 120 Ω and were bonded directly inside the grooves using Cyanoacrylate adhesive. This allowed the induced strain in the rock bolts to be directly transferred to the coupled strain gauges, and the resulting electrical signals were received in the data acquisition system. Due to space limitations in passing the strain gauge wires, the strain gauges were installed alternately in each groove with a distance of 50 mm between them. To protect the strain gauges and lead wires, an organic and non-acidic sealant was applied to fully cover the instruments and the grooves. Figure 5 schematically illustrates the position of the strain gauges and the instrumentation arrangement used for the preparation of the pullout specimen with a 400 mm encapsulation length. This arrangement was followed for the preparation of all pullout specimens with varying encapsulation lengths, although the number of mounted strain gauges varied. Three, four, five, seven, and nine strain gauges were applied to bolts with 100, 150, 200, 300, and 400 mm encapsulation lengths, respectively. A tensile strength test was also conducted to determine the tensile properties of the bolt with opposite grooves (Fig. 6). Creating the grooves alters the bolt's yield and ultimate load capacities to 205 kN and 285 kN, respectively.

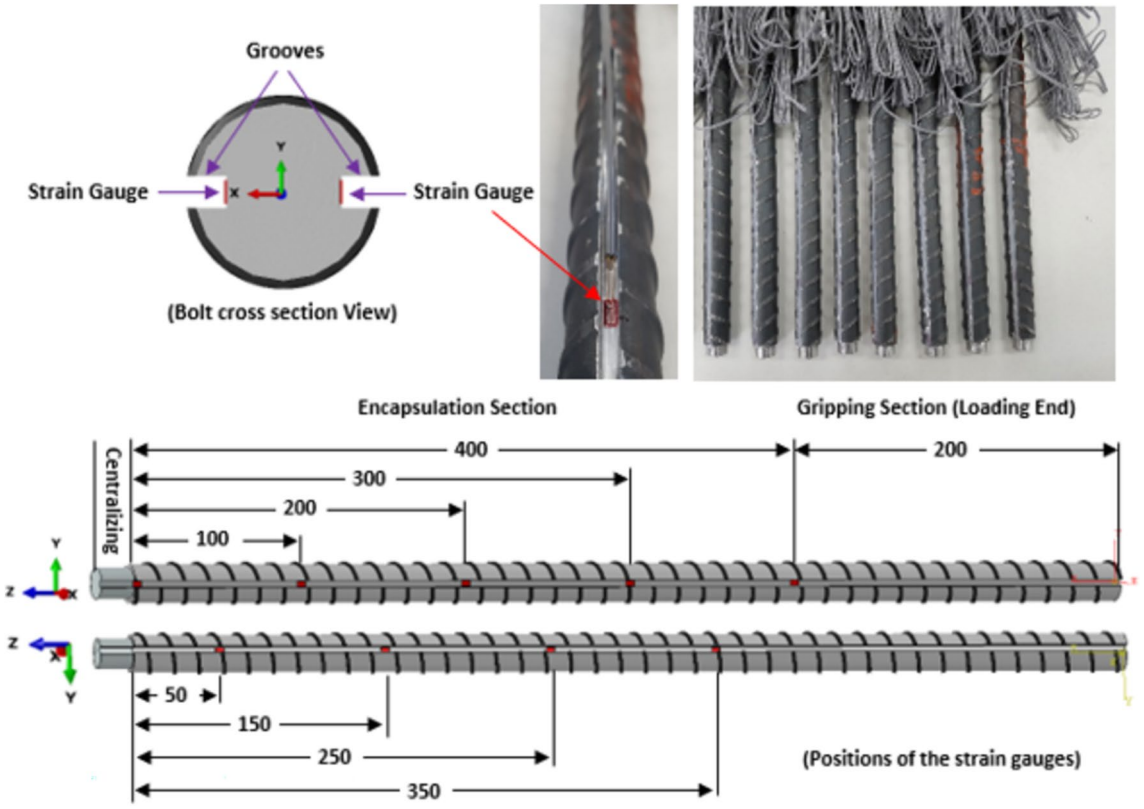

Fig. 5 Bolt instrumentation with 400 mm encapsulation. Red colored squares are strain gauges

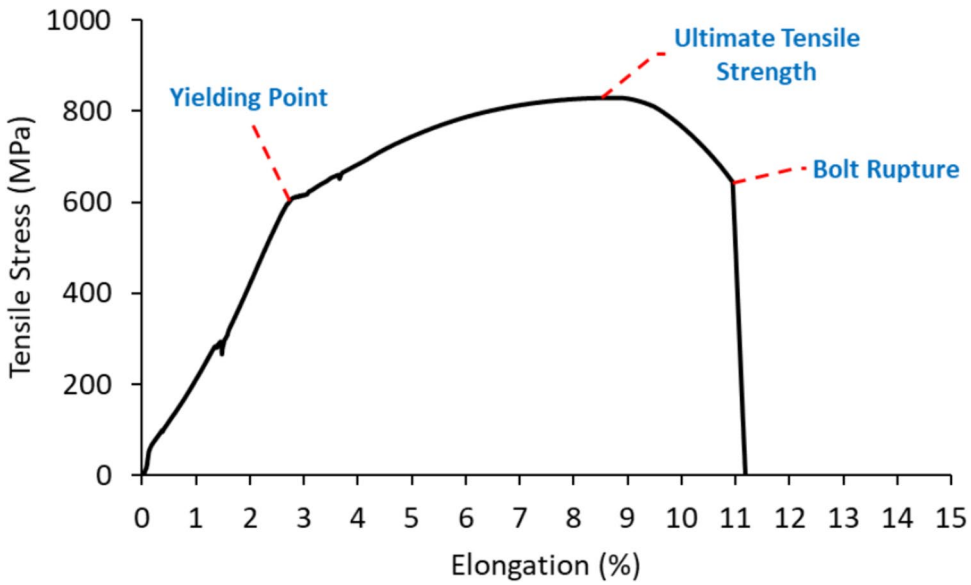

Fig. 6 Tensile behavior of the grooved bolts

2.2 Pullout Tests

For the pullout tests, an instrumented Coal Bolt was fully bonded inside the holes that were created in the concrete cylinders using G1, G2, R1, R2, and R3. The arrangement of the pullout tests is presented in Table 4. As shown, the testing campaign includes 17 pullout tests that were conducted on specimens with three types of concrete, five types of bonding agents, and five different encapsulation lengths. A specific jig was designed for performing the pullout tests

Table 4 Overview of the pullout test program

Series	Specimen	Encapsulation length (mm)	Grout type	Main failure	Concrete grade
A	A1	100	G1	Slip	M40
	A2	200	G1	Slip	M40
	A3	300	G1	Bolt rupture	M40
	A4	400	G1	Bolt rupture	M40
B	B1	100	R2	Slip	M40
	B2	200	R2	Slip	M40
	B3	300	R2	Slip	M40
	B4	400	R2	Bolt rupture	M40
C	C1	150	G2	Slip	M20
	C2	150	G2	Slip	M40
	C3	150	G2	Slip	M60
D	D1	150	R1	Slip	M20
	D2	150	R1	Slip	M40
	D3	150	R1	Slip	M60
E	E1	150	R3	Slip	M20
	E2	150	R3	Slip	M40
	E3	150	R3	Slip	M60

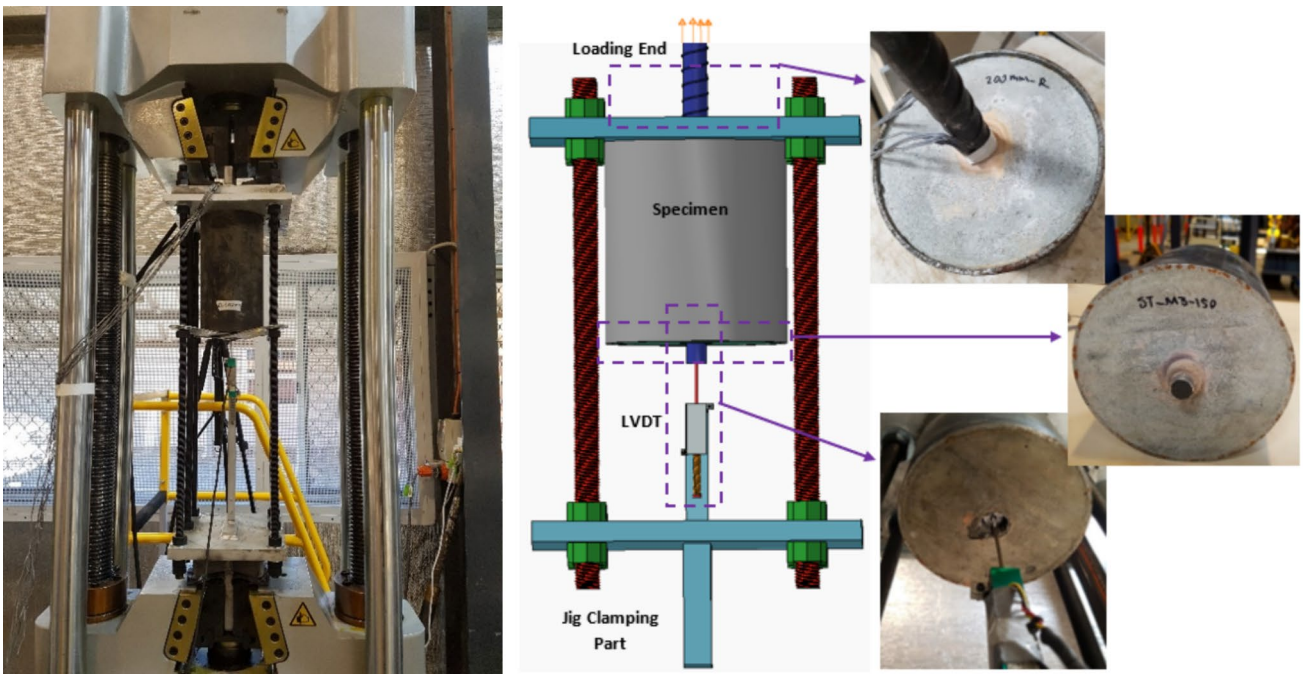

Fig. 7 Pullout test arrangement including the jig and specimen and the adjusted LVDT adjusted on the end of the bolt

(Fig. 7). Initially, the jig was clamped onto the lower crosshead of a 1000 kN universal tensile machine, and then the specimens were placed inside the jig. The loading end of the bolt was passed through a 150 mm hole in the upper plate of the jig and then gripped by the machine's jaws. Two displacement sensors, LVDTs, were employed to monitor and measure the displacement of the bolt. One was located on the tensile machine's upper crosshead, while the other one was located underneath the specimen (Fig. 7). The upper LVDT was used to measure the displacement of the bolt from the loading end, while the lower one was used for measuring the slip of the free end of the bolt. This arrangement was designed to monitor the differences between displacements and/or deformations that developed at the loading and free

ends. Once the specimen was set up, the strain lead wires of the strain gauges were connected to the data acquisition system, and the bolt was pulled out by a loading rate of 1 mm/s.

3 Pullout Test Results and Discussion

Table 4 provides an overview of the pullout testing program, including the encapsulation length, grout type, concrete grade, and overall failure mode. To simplify the analysis of the test results, the specimens were grouped into series labeled A, B, C, D, and E. The pullout test results will be discussed in Sect. 3.1, which focuses on the effects of the encapsulation length on the pullout results, and Sect. 3.2, which presents the results of pullout tests related to the grout types and the influence of the host medium on the performance of fully embedded rock bolts.

3.1 Effect of Embedment Length

Eight pullout tests were conducted on specimens with varying embedment lengths, ranging from 100 to 400 mm, and were encapsulated using two different bonding agents, namely G1 and R2. However, all tests used concrete grade M40 for the host medium. The results are presented below.

3.1.1 Load–Displacement Relation

Figure 8 shows the load–displacement curves for series A and B specimens. Bolt rupture occurred in specimens A3, A4, and B4, while the other specimens showed full slip debonding failure. Bolt B3 was pulled out with a force close to the ultimate tensile strength of the bolt just before the necking phenomenon occurred in the bolt. Furthermore, bolt B3 was pulled out with a force above its yielding capacity. According to the results, the load–displacement relation can be divided into three general categories regardless of the type of bonding agent (Høien et al. 2021). These are: bolt slip occurs when the pullout load level is less than the yielding capacity of the bolt, bolt slip occurs when the pullout load is between the yielding capacity and ultimate tensile capacity of the bolt, and lastly, the system fails due to bolt rupture.

The first type of failure is observed in A1, A2, B1, and B2, in which bolt slip takes place before the pullout load reaches the yield load of the bolt. This type of failure is associated only with the elastic deformation of the bolt bar, and thus plastic deformation shall not be observed. As shown in Fig. 8, the displacement increases with load linearly until reaching a specific point after which the load–displacement relationship is not linear, and the slope of the curve decreases continuously till reaching the peak load. It was interestingly found that the axial pullout stiffness (ratio of load over displacement) of the curves in the initial linear stage for all A1-A4 and B1-B4 specimens is equivalent and equal to 35 kN/mm regardless of the type of bonding agent and encapsulation length. Further analysis of the results indicates that the initial linear growth of the load–displacement (e.g., section A in Fig. 8a) is associated with the elastic deformation of the whole system. This indicates that, within this linear section, the bolt-grout system has not sustained any damage. Therefore, releasing the load within this range can return the system to its initial state without permanent deformation or damage. It should be noted that the extent of the linear section varies depending on the encapsulation length and the encapsulation material. However, critical plastic deformation due to debonding or failure at bonding or surrounding material initiates once the change in the slope of the curve appears (e.g., section B). To support this assumption, loading of the test A4 was paused once the load reached 150 kN, and the specimen was examined in detail. No slip failure was observed in the specimen. Nevertheless,

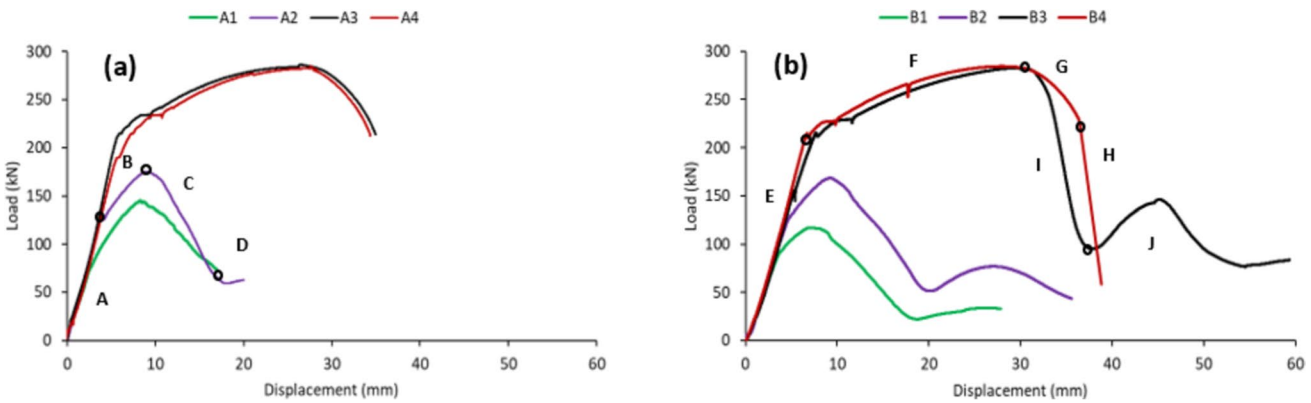

Fig. 8 Load–displacement curves of pullout tests for the specimens having anchorage length 100–400 mm; **a** encapsulated with cementitious grout G1, and **b** encapsulated specimens with resin R2

a cone-shaped failure was obvious in the concrete which can be neglected. Therefore, it is concluded that the initial linear growth (section A) in load–displacement can be considered as non-slip elastic deformation, while the section between the end of the linear section and the peak point (section B) is comprised of both elastic deformation and slip failure which is termed slip-elastic deformation. Slip-elastic deformation ends up with peak load followed by continuous reduction in the load vs. displacement (section C). At this stage, the bonding material is sheared off continuously till there is no obstacle against the slip of the bolt. When irregularities at the bolt-grout interface are all smoothed, only friction remains between the contacts as the effective resistance, and if the encapsulation length remains constant, the frictional residual strength will keep steady (section D). As shown in Fig. 8, a higher encapsulation length provides higher residual strength. On the contrary, the load–displacement curves of A3, A4, and B4 resemble the curve of a bolt tensile test, including elastic, strain hardening, necking, and final rupture of the bolt (sections E, F, G, and H in Fig. 8b). However, a portion of the total force was utilized for localized debonding at the collar's vicinity, in addition to creating cone failure in the concrete. This behavior indicates that increasing the anchorage length beyond a certain point does not enhance the bolt's performance. The B3 bolt, with 300 mm of anchorage, was pulled out when the load approached the ultimate tensile capacity of the bar. The load–displacement curve is similar to the B4 curve in the elastic and strain-hardening parts (sections E and F). However, just before necking, the system begins to debond along the encapsulation length, leading to continuous reduction of the load–displacement (section I) until reaching the frictional residual strength (section J).

3.1.2 Embedment Length vs. Pullout Characteristics Relationship

Figure 9 shows the relation between the embedment length and peak pullout load obtained from the test series A and series B. The data points are the values obtained from the pullout tests, but the trend lines have been enveloped to delineate the approximate patterns and predict values beyond the immediate data set. The tree-line trends were derived from experimental pullout data points, including yield load strength and tensile load strength. For instance, the trend line for series B was established by connecting points 1 and 2, then intersecting the yield load limit at point 3. Subsequently, a line was drawn to connect to point 4 (ultimate embedment length), followed by a horizontal line representing the bolt's ultimate load capacity (iii). The embedment length corresponding to point 3, which is 268 mm, signifies the critical embedment length at which the pullout capacity equals the yield capacity of the bolt. Similarly, after applying the same procedure to series A data points, it was observed that trends i and i' are parallel, suggesting that the second stage for series A tests can be delineated by drawing a line parallel to ii, potentially estimating the ultimate embedment length (point X). Point X determines the embedment length necessary to achieve ultimate pullout capacity based on series A testing parameters, revealing it to be 282 mm. Stage (i) covers embedment lengths below the bolt yield capacity threshold, stage (ii) spans embedment lengths corresponding to pullout capacities between yield strength and ultimate tensile strength of the bolt, and stage (iii) encompasses embedment lengths equal to or greater than the critical embedment length, where pullout capacity equals the bolt's ultimate tensile strength. The findings cover

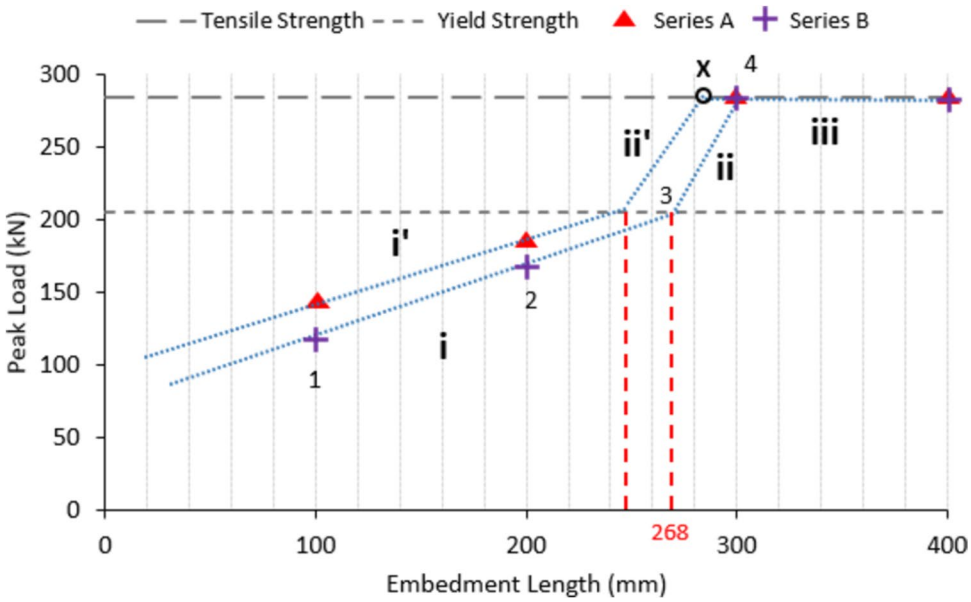

Fig. 9 Relationship between embedment length and peak pullout strength

Table 5 Summary of the pullout tests results for series A and B

Grout	Specimen	Embedment length (mm)	Peak load (kN)	Displacement at peak (mm)	Residual strength (kN)	Rate of ascending in Sect. 1 (kN/mm)	Rate of ascending in Sect. 2 (kN/mm)	Descending rate (kN/mm)
G1	A1	100	143	8.4	50.3	34.5	12.21	9.9
	A2	200	176	8.9	64.5	34.5	12.18	15.56
	A3	300	285	27.7	0	34.5	N/A	N/A
	A4	400	285	27.6	0	34.5	N/A	N/A
R2	B1	100	117	6.8	33.6	33.3	7.23	10.09
	B2	200	168	9.4	49.2	33.3	10.5	11.97
	B3	300	284	28	81	33.3	N/A	N/A
	B4	400	284	28	0	33.3	N/A	N/A

a wide range of performances of rock bolts associated with the embedment length and emphasize the significance of stage (ii), where a small increase in the embedment length (≈32 mm in series B) causes a significant improvement in the performance of the bolt (80 kN in series B). The yield ratio, typically ranging from 0.7 to 0.85, significantly influences the critical embedment length and the slope of the trend line in stage (ii). Higher yield ratios correspond to increased embedment lengths and steeper trend line gradients, amplifying the impact of even small increases in embedment length on pullout capacity. The critical embedment length for series A (point 5) is approximately determined by the enveloped trend line at 247 mm. The range of the embedment length for stages (i), (ii), and (iii) of series A was found approximately to be < 247 mm, 247–282 mm, and > 282 mm, respectively.

Table 5 summarizes the pullout characteristics of the series A and B tests. In general, the higher the embedment length, the higher the ultimate capacity, stiffness, and frictional residual strength. For instance, in series A, an increase in the embedment length from 100 to 200 mm and from 200 to 300 mm increases the ultimate bearing capacity by 23% and 62%, respectively. This improvement for series B was measured at 43% and 69%. It can also be seen that an increase in the embedment length shifts the corresponding displacements at the peak loads to the right. Comparison of the results presented in Fig. 8 and Table 5, also indicates that, for the same embedment length, the bearing capacity of grouted rock bolts using G1 (A series) is higher than that of bolts encapsulated using R2 bonding agent, even though the compressive strength of G1 is 15% less than that of R2 (Fig. 4). This signifies that the compressive strength of the bonding agent should not be considered as the sole parameter influencing the bearing capacity of the system. The effect of mechanical characteristics of the bonding materials on the behavior of rock bolts will be discussed in detail in Sect. 1.3.

3.2 Bond Stress Distribution Along the Embedment Length for Series A and B

Bond refers to the shear resistance induced between the bolt bar and bonding materials in response to the pullout

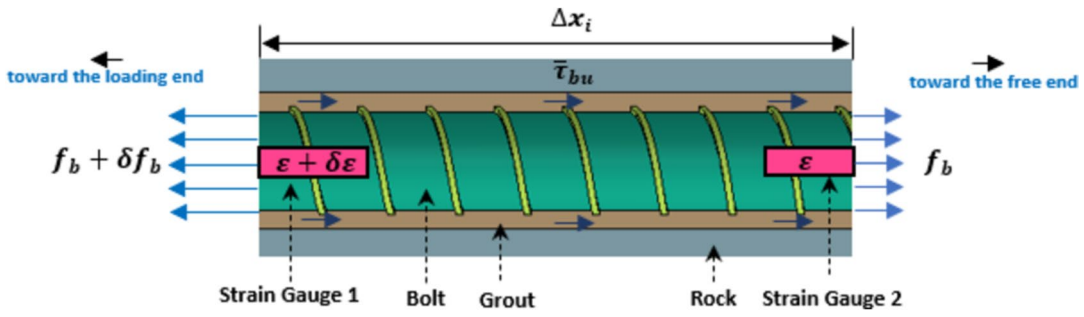

Fig. 10 Stress equilibrium in a length of embedded rock bolt

load. It has been shown that the bond stress generated at the bolt-grout interface and along the embedment length of a fully grouted rock bolt is non-uniform, although it is common to assume a uniform bond stress distribution for short embedment specimens. Bond stress distribution can be technically quantified by measuring the longitudinal elongation degrees of the bolt along the embedment length using sensors such as strain gauges. Figure 10 schematically shows the stress equilibrium at a section of a grouted bolt with a length of Δx. Assuming three main conditions, i.e., (1) a uniform bond stress distribution along Δx, (2) no energy loss in other forms such as creating fractures, cracks, and damages, and (3) no deformation in the host rock, we can write the following force equilibrium for Fig. 10:

$$f_b + \delta f_b = f_b + \overline{\tau}_{bu}\left(\pi d_b \Delta x\right), \tag{1}$$

where $f_b + \delta f_b$ is the force subjected at strain gauge 1, f_b is the bolt force acting at strain gauge 2, $\overline{\tau}_{bu}$ is the induced interfacial shear stress at the bolt-grout interface, d_b is the nominal diameter of the bolt, and Δx is the distance between the strain gauges.

Applying the constitutive equation ($\sigma = \varepsilon.E$) in Eq. (1) the following equation is achieved:

$$(\varepsilon + \delta\varepsilon)Ea_b = \varepsilon E a_b + \overline{\tau}_{bu}\left(\pi d_b \Delta x\right), \tag{2}$$

where $\varepsilon + \Delta\varepsilon$ is the strain value measured by strain gauge 1, E is the elastic modulus of the bolt, a_b is the cross area of the bolt and ε is the strain value measured by strain gauge 2.

By simplifying Eq. (2), interfacial bond stress along Δx can be calculated as follows:

$$\overline{\tau}_{bu} = \frac{\delta\varepsilon E d_b}{4\Delta x}. \tag{3}$$

Therefore, monitoring the elongation of bolts along the embedment length due to the pullout load is an effective way to determine the interfacial bond stress distribution. This information is essential for developing efficient constitutive models for the axial performance of anchored bolts. It should be noted that the equations presented for a full-scale anchored bolt are only applicable if the free end of the bolt is assumed to be fixed in the loading direction and restrained from any displacement. The reliability of the data presented in this section, as compared to similar studies in the literature, lies in three factors: firstly, the presented data covers the whole pullout process, rather than just partial data. Secondly, most of the possible failure types in rock bolting are individually investigated. Finally, the combined effect of other parameters such as grout and host rock quality was also investigated.

Figures 11 and 12 illustrate the development of interfacial bond stress along the encapsulation length, with displacement measured at the loading end for test series A and B,

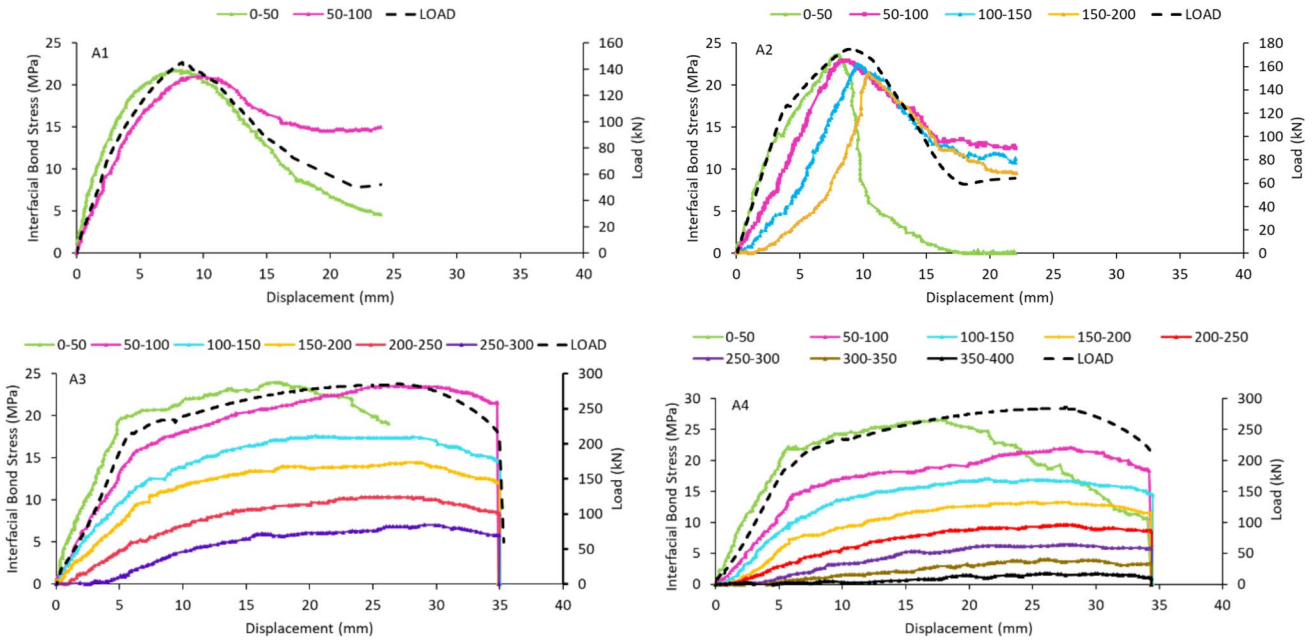

Fig. 11 Bond stress and displacement relationship in series A tests at various sections along the embedment. Color-coded curves depict the evolution of interfacial bond stress relative to the displacement at the loading end of the bolt across different sections along its length. For instance, green curves represent bond stress within the 0–50 mm section of the bolt, while pink curves correspond to the 50–100 mm section. Dashed lines present the pullout load versus displacement curves shown in Fig. 8

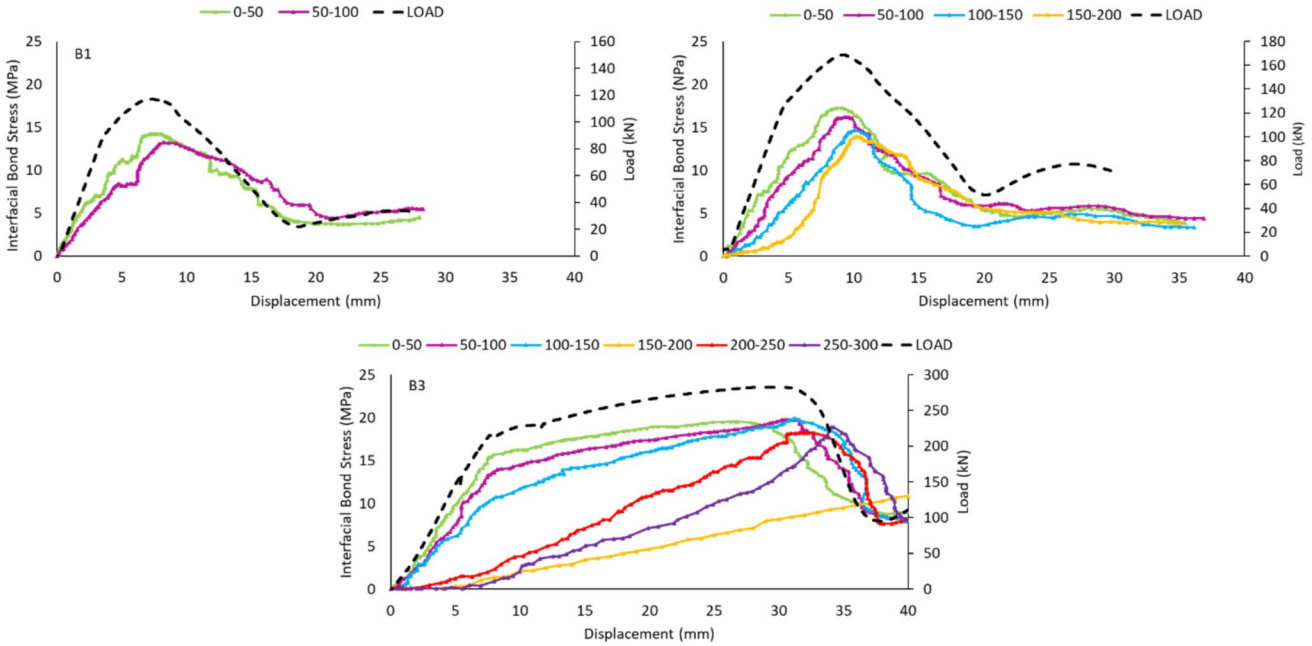

Fig. 12 Bond stress and displacement relationship in series B tests at various sections along the embedment. Color-coded curves depict the evolution of interfacial bond stress relative to the displacement at the loading end of the bolt across different sections along its length. For instance, green curves represent bond stress within the 0–50 mm section of the bolt, while pink curves correspond to the 50–100 mm section. Dashed lines present the pullout load versus displacement curves shown in Fig. 8

respectively. As shown the distribution of bond stress relies on the failure mode of the system, such as shank rupture and failure at the bolt-grout interface. However, in most cases, the bond stress distribution-displacement development aligns well with the pullout load–displacement curves. This suggests that the induced bond stress increases with the increase in the pullout load, irrespective of the embedment length and distance. Furthermore, the results indicate that the maximum bond stress along the embedment length may not be attained at the maximum pullout load, and it can occur before or after these points.

During tests A1 and A2, where fully debonding of the bolt was achieved, the peak bond stress for the instrumented sections ranged between 21 and 23.5 MPa. The analysis of the results shows that debonding of the bolts initially started from the loading end and then extended towards the free end of the bolt, accompanied by a slight displacement of the bolts. In test A1, the highest magnitude of bond stress at the 0–50 mm section occurred when the pullout load reached 139 kN, which is 97.2% of the peak load. Similarly, in the 50–100 mm section of test A1, the maximum bonding stress of 21.09 MPa was achieved when the pullout load reduced to 136 kN (95.1% of the peak load). In test A2, the peak bond stress for the 0–50, 50–100, 100–150, and 150–200-mm sections was measured as 23.58, 22.9, 22.5, and 21.46 MPa, respectively, at pullout loads of 170, 175, 162, and 156 kN. These results demonstrate that debonding in the vicinity of the loading end begins before the pullout load reaches its peak value. However, the debonding of the deeper sections occurs at the peak load or in the post-peak part of the loading. The bond stress curve for the 0–50 mm section of test A2 displays an unusual behavior where the bond stress settles at zero level at the displacement of 17.5 mm. Examination of the specimen after the completion of the test revealed that a cone-shaped damage at the grout and concrete caused 29 mm of the bolt to become unembedded, and then further slip of the bolt continuously contributed to the extension of the unembedded section until 17.5 mm of slip, after which the strain values became identical along the 0–50 mm section, resulting in zero bond resistance. A similar behavior was observed in test B2. However, the bond stress curve reached a zero value at higher displacement, which was due to the depth of the cone damage being 13 mm. In both A3 and A4 tests, the bond stress curve for the 0–50 mm section (the green line) switched to a descending trend at the displacement of 15–20 mm, which can be attributed to the initiation and propagation of circumferential cracks created at the grout.

Table 6 presents the magnitudes of interfacial bond stress induced at 50, 100, 150, and 200 kN pullout loads for tests A1–A4 and B1–B3. The results show that as the embedment length increases, the subjected pullout load diffuses over a longer length. Due to the longer bonded length, stress concentration is minimized. This means that at a specific level of pullout load, the induced interfacial bond stress at

Table 6 Bond stress magnitudes at different pullout loads and sections along the embedment length for tests A1–A4 and B1–B3

	Sections	0–50	50–100	100–150	150–200	200–250	250–300	300–350	350–400	Average
	50 kN									
Series A	A1	10.41	6.51							8.46
	A2	6.86	3.36	1.29	0					2.87
	A3	6.47	3.88	3.23	2.46	0.77	0.1			2.81
	A4	8.56	3.15	1.41	0.54	0.36	0.36	0.019	0.016	1.8
Series B	B1	5.65	3.68							4.66
	B2	5.15	2.7	1.52	0.23					2.4
	B3	3.86	3.09	2.7	1.54	0.64	0.1			1.98
	100 kN									
Series A	A1	14.06							16.14	18.22
	A2	6.99	4.40	1.16					6.34	12.82
	A3	8.29	6.47	4.66	2.07	0.25			5.58	11.78
	A4	6.31	4.57	2.12	1.43	0.38	0.25	0.12	3.47	12.59
Series B	B1	8.15							9.33	10.52
	B2	6.93	3.83	1.11					4.99	8.12
	B3	5.79	5.02	3.73	0.9	0.38			3.86	7.34
	150 kN									
Series A	A2	19.43	17.22	11.01	4.66					13.08
	A3	15.93	10.36	8.16	6.08	2.97	0.38			7.31
	A4	17.14	9.47	7.37	4.41	2.14	0.92	0.39	0.28	5.26
Series B	B2	13.37	11.03	8.57	4.82					9.44
	B3	10.3	7.98	6.44	5.28	1.41	0.51			5.32
	200 kN									
Series A	A2	13.08								
	A3	7.31	19.68	13.47	9.97	7.38	4.27	1.03		
	A4	5.26	22.22	14.55	10.53	7.57	3.56	1.99	0.94	0.29
Series B	B2	9.44								
	B3	5.32	13.91	11.98	9.79	6.82	1.93	0.64		

The stresses are measured in MPa

a particular section is lower in a longer embedment length. For example, at 50 kN of pullout load, the bond stress at the first section (0–50 mm) for A1, A2, A3, and A4 was measured at 10.41, 6.86, 5.47, and 4.65 MPa, respectively. Similar conditions can be noted at higher load levels and at other sections as well. This becomes more critical when comparing the distribution of bond stress of specimens with different bonding agents (e.g., A1 and B1, A2 and B2, and A3 and B3). The results indicate that at a particular level of pullout load, series B tests generally exhibited lower bond stresses compared to series A. For instance, at 100 kN, the bond stress was recorded at 14.06 and 8.15 MPa for A1 and B1 at the 50–100 mm section, respectively. Similarly, at 150 kN and 100–150 mm section, bond stress was measured at 8.16 and 6.64 MPa for A3 and B3, respectively. The reason can be attributed to the mechanical properties of the bonding agent, in particular, the modulus of elasticity.

Figure 13 depicts the bond stress profile along the embedment length at load levels of 50%, 75%, and 100% of the peak load, as well as at the post-peak residual strength for the tests that were fully debonded (i.e., A1, A2, B1, B2, and B3). The results indicate that, generally, the bond stress at a specific pullout load level decreases from the loading end to the free end, although there are exceptions, particularly in the post-peak residual bond strength of A2, B2, and B3. In A2, the 150–200 mm section does not present bond resistance due to the cone-shaped damage created at the collar's vicinity after the peak load was achieved. The depth of the cone damage for A2 was measured at 43 mm from the specimen surface, fully covering the 150–200 mm section and 13 mm of the 100–150 mm section. Similar cone-shaped damage was observed in A3, A4, B2, B3, and B4, but with different depths, which will be discussed in detail in Sect. 3.1.4. Additionally, it is evident that the initial residual bond strength in the sections towards the free end is higher. This may be due to the fact that the debonding damage to the encapsulation and/or radial dilation, as a consequence of bolt elongation/slip,

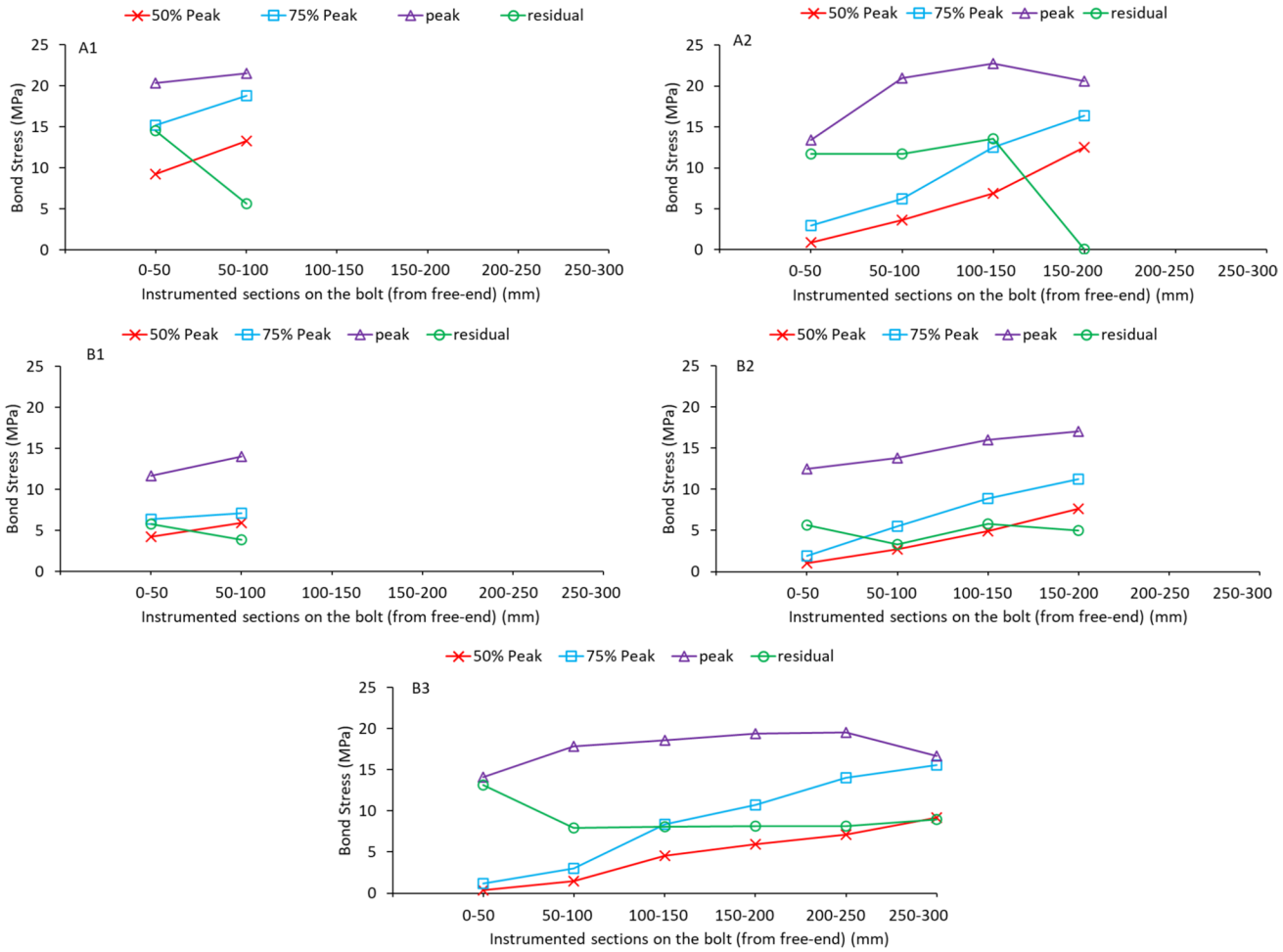

Fig. 13 Bond stress profile along the embedment length corresponding to loads of 50% of peak load, 75% of peak load, peak load, and residual capacity

is less at the vicinity of the free end, while the sections closer to the loading end are completely damaged at that specific elongation.

Moreover, it is interesting to note that the initial residual bond stress is higher than the bond stress induced by 75% of the peak load at the 0–50 mm section for the specimens shown in Fig. 13. The results show that the minimum bond stress is achieved at the vicinity of the free end when the pullout load is equal to or less than the peak load. In A1, B1, and B2, the maximum bond stress corresponding to the peak load was found at the section close to the loading end, while in A2 and B3, it was measured at the 100–150 mm and 200–250 mm sections, respectively. This indicates that in the latter specimens, debonding of the embedded section at the collar occurred before the pullout load reached the peak load.

3.2.1 Bond Stress Distribution vs Mechanical Properties of Encapsulation Materials

Figure 14 illustrates the potential response of rock bolting systems embedded in bonding materials with different mechanical characteristics when subjected to pullout forces. In any type of bonding material encapsulating rock bolts are loaded axially in pull or push out, as shown in Fig. 14a, the bonding agent serves to transfer axial load from the bolt to the host rock through bond stresses distributed along the encapsulation length. Figure 14b shows the equilibrium balance of the differential element in the embedded region. The following basic equilibrium equations can be presented based on this statistically indeterminate problem:

$$\frac{\mathrm{d}p(x)}{\mathrm{d}x} = \pi d_b \tau_b(x) \tag{4a}$$

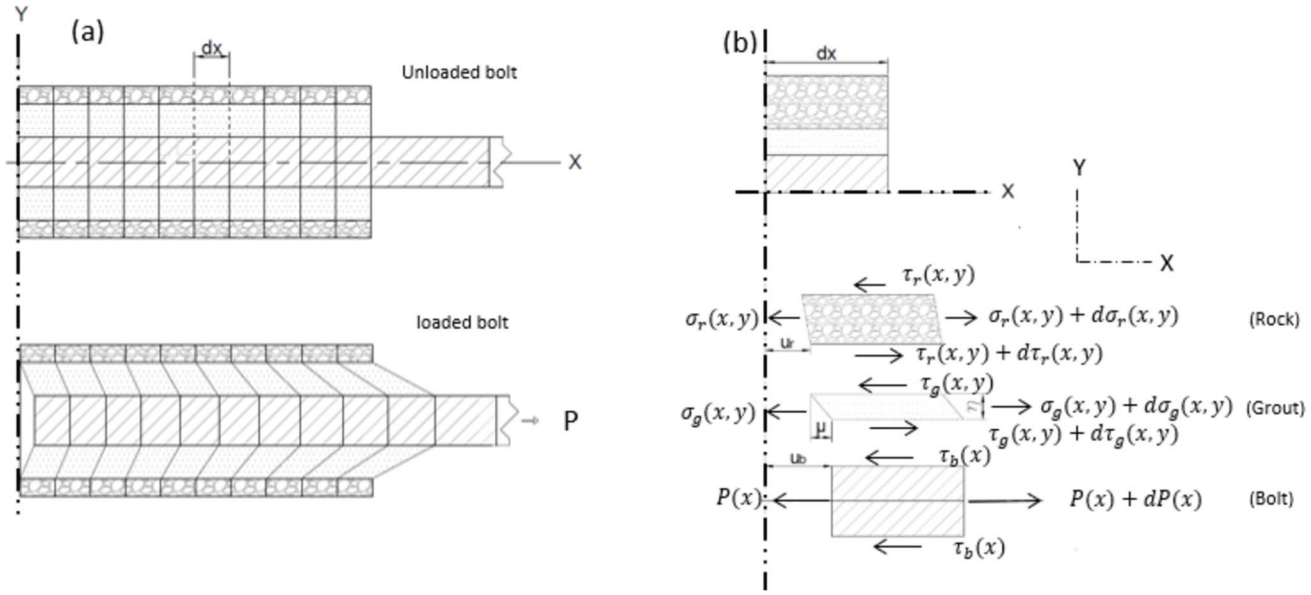

Fig. 14 **a** Encapsulated bolt before and after subjecting to a tensile load, and **b** deformation and stress distribution in an infinitesimal length in the bolt, grout and rock elements

$$\frac{\partial \sigma_g(x,y)}{\partial x}+\frac{\partial \tau_g(x,y)}{\partial y}=0 \tag{4b}$$

$$\frac{\partial \sigma_r(x,y)}{\partial x}+\frac{\partial \tau_r(x,y)}{\partial y}+X_r=0, \tag{4c}$$

where $p(x)$ is the axial force subject to the bolt at the position of x, $\tau_b(x)$ is the resultant bond stress on the bolt, $\sigma_g(x,y)$ is the axial stress in the bonding agent parallel to the rock bolt at (x,y), $\tau_g(x,y)$ is the induced shear stress in the bonding agent and at the position of (x,y), $\sigma_r(x,y)$ is the axial stress in the host rock parallel to the rock bolt at (x,y), $\tau_r(x,y)$ is the shear stress in the host rock and X_r is the body force of the host rock acting at x direction. In the above differential equations, the body force of the bolt and the bonding agent are ignored as they are relatively small compared to the host rock. Since it is difficult to solve the problem only by the existing equilibrium equations and boundary conditions, the basic shear-lag model as the most fundamental concepts in the load transfer mechanism between bonded members is adopted (Yang et al. 2008). The bonding agent is relatively thin compared to the bolt and the host rock thus it can be assumed that the bonding agent does not carry significant axial forces, therefore $\frac{\partial \sigma_g(x,y)}{\partial x}=0$ and $\tau_g\left(x,y\middle|\begin{matrix}r_b+\eta\\ r_b\end{matrix}\right)=\tau_b(x)$. The constitutive laws and shear-lag model for fully encapsulated rock bolts can be expressed as follows.

$$\tau_b(x)=G_g\gamma_{xy}=G_g\left(\frac{\partial (u_g)_x}{\partial y}+\frac{\partial (u_g)_y}{\partial x}\right), \tag{5}$$

where G_g and γ_{xy} are the shear modulus of the bonding agent and the shear strain of the bonding agent in the xy plane, respectively. $(u_g)_x$ and $(u_g)_y$ are the displacement of the bonding element at the x and y directions, respectively. u_y is relatively much smaller than u_x due to the lower magnitude of resultant stress parallel to the y axis, thus it can be neglected for simplifications.

$$\tau_b(x)=G_g\left(\frac{u_b(x,0)-u_r\left(x,r_b+\eta\right)}{\eta}\right), \tag{6}$$

where G_g is the shear modulus of the bonding agent and η is the thickness of the bonding agent. u_b and u_r are displacement of the bolt and host rock in the direction of loading, respectively as shown in Fig. 14b. Taking derivative from the Eqs. (4a) and (6) with respect to x yields:

$$\frac{\mathrm{d}^2P(x)}{\mathrm{d}x^2}=2\pi r_b\frac{\mathrm{d}\tau_b(x)}{\mathrm{d}x} \tag{7}$$

$$\begin{aligned}\frac{\mathrm{d}\tau_b(x)}{\mathrm{d}x}&=\frac{G_g}{\eta},\left(\frac{\mathrm{d}u_b(x,0)}{\mathrm{d}x}-\frac{\mathrm{d}u_r\left(x,r_b+\eta\right)}{\mathrm{d}x}\right)\\&=\frac{G_g}{\eta}\left(\varepsilon_b(x,0)-\varepsilon_r\left(x,r_b+\eta\right)\right)\end{aligned} \tag{8}$$

where $\varepsilon_b(x,0)$ is the bolt strain and $\varepsilon_r\left(x, r_b+\eta\right)$ is the host rock strain at the edge of $r_b+\eta$ induced by applying an axial load of $P(x)$ at the position of x.

$$\varepsilon_b(x,0)=\frac{P(x)}{\pi r_b^2 E_b}, \tag{9}$$

where E_b is the elastic modulus of the bolt. Considering the shear modulus of the host rock as G_r, the distributed shear stress and axial strain in the host rock can be expressed as:

$$\tau_{rx}(x,y)=G_r\gamma_{xy}=G_r\left(\frac{\partial(u_r)_x}{\partial y}+\frac{\partial(u_r)_y}{\partial x}\right). \tag{10}$$

By neglecting the shear deformation in y direction, ε_r is expressed as

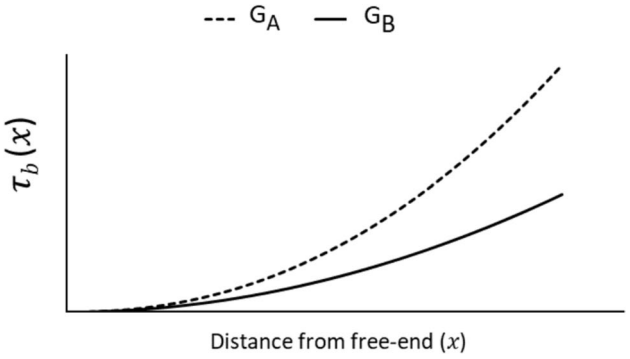

Fig. 15 Schematic of the effect of the shear modulus of the bonding materials (G) on the bond stress distribution based on Eq. (15) for two different types of bonding materials including A and B where $G_A > G_B$

$$\varepsilon_{rx}\left(x, r_b+\eta\right)=\frac{\sigma_{rx}\left(x, r_b+\eta\right)}{E_r}+\frac{R\tau_{rx}\left(x, r_b+\eta\right)}{\Delta x.G_r}, \tag{11}$$

where $\varepsilon_r\left(x, r_b+\eta\right)$ is the strain of the host rock at the grout-rock interface, σ_{rx} is the stress parallel to the loading direction, and E_r,R and Δx are the elastic modulus, the thickness of the host rock and the length of the element, respectively. Substituting Eqs. (8), (9), (10), and (11) into Eq. (7) yields:

$$\frac{\mathrm{d}^2P(x)}{\mathrm{d}x^2}=\frac{2\pi r_b G_g}{\eta}\left(\frac{P(x)}{\pi r_b^2 E_b}-\left(\frac{\sigma_{rx}\left(x, r_b+\eta\right)}{E_r}+\frac{R\tau_{rx}\left(x, r_b+\eta\right)}{\Delta x.G_r}\right)\right) \tag{12}$$

$$\frac{\mathrm{d}^2P(x)}{\mathrm{d}x^2}-\phi^2P(x)=f\left(\sigma_{rx},\tau_{rx}\right), \tag{13}$$

where $\phi=\sqrt{\frac{2G_g}{\eta r_b E_b}}$.

Equation (13) is a second-order linear homogeneous differential equation with a non-homogeneous term on the right-hand side. To solve this differential equation, $f\left(\sigma_{rx},\tau_{rx}\right)$ is assumed to be zero, thus:

$$P(x)=C_1e^{\phi x}+C_2e^{-\phi x}, \tag{14}$$

where C_1 and C_2 are constants determined by initial and boundary conditions. The expression of $\tau_b(x)$ is as follows:

$$\tau_b(x)=\phi(C_1e^{\phi x}-C_2e^{-\phi x}). \tag{15}$$

The distribution of bond stress τ_b is schematically illustrated in Fig. 15 based on Eq. (15). This equation indicates that when investigating the effect of encapsulation materials on the performance of fully embedded rock bolts while keeping other factors identical, the shear modulus of the encapsulation material has the most significant impact on the

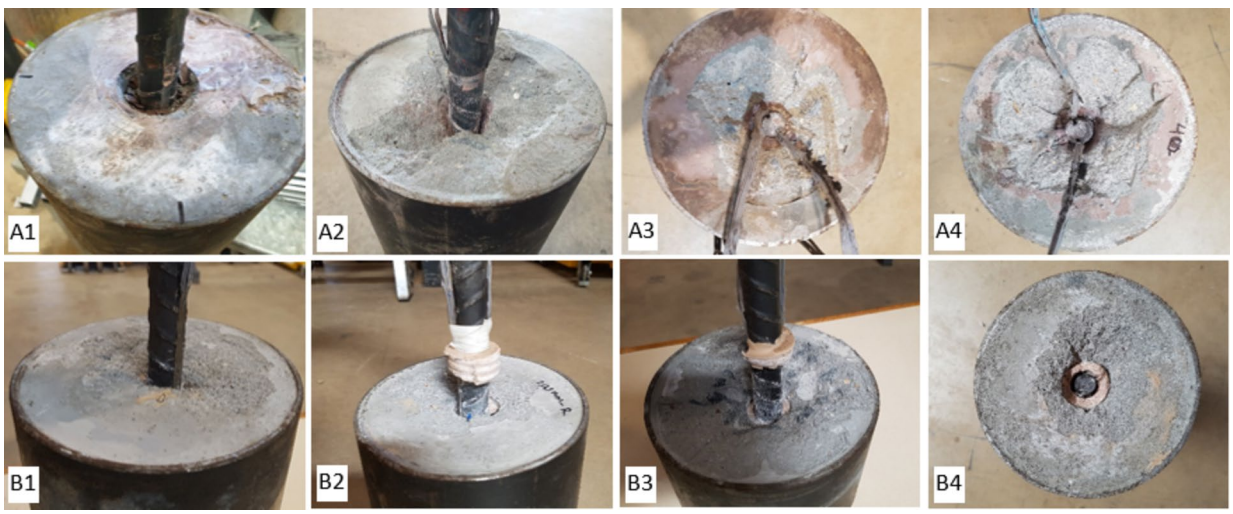

Fig. 16 Cone-shape damage at the loading end of the specimens with different embedment lengths

axial load transfer along the encapsulation length and, consequently, the distribution of induced bond stress at the bolt grout interface. As seen, an increase in the shear modulus of the bonding material results in an increase in the magnitude of bond stress along the embedment length. This is consistent with the experimental results presented in Figs. 11 and 12 and Table 6, as discussed above, since the shear modulus of the bonding agents used in the A and B series of tests is 11.7 and 2.9 GPa, respectively.

3.2.2 Failure Pattern of the Specimens with Different Embedment Lengths

During pullout testing, the primary failure modes observed in the samples were bolt rupture and debonding at the bolt-grout interface. Visual inspections further identified cone-shaped damage at the host rock. While not the predominant failure mode, this additional damage could significantly influence the overall behavior of the samples. The cone-shaped damage is visible in all specimens except A1, but the depth and area of the damage differ, as shown in Fig. 16. From observations and further investigations, it can be concluded that the intensity of the cone-shaped damage may be associated with two main factors: (1) the maximum pullout

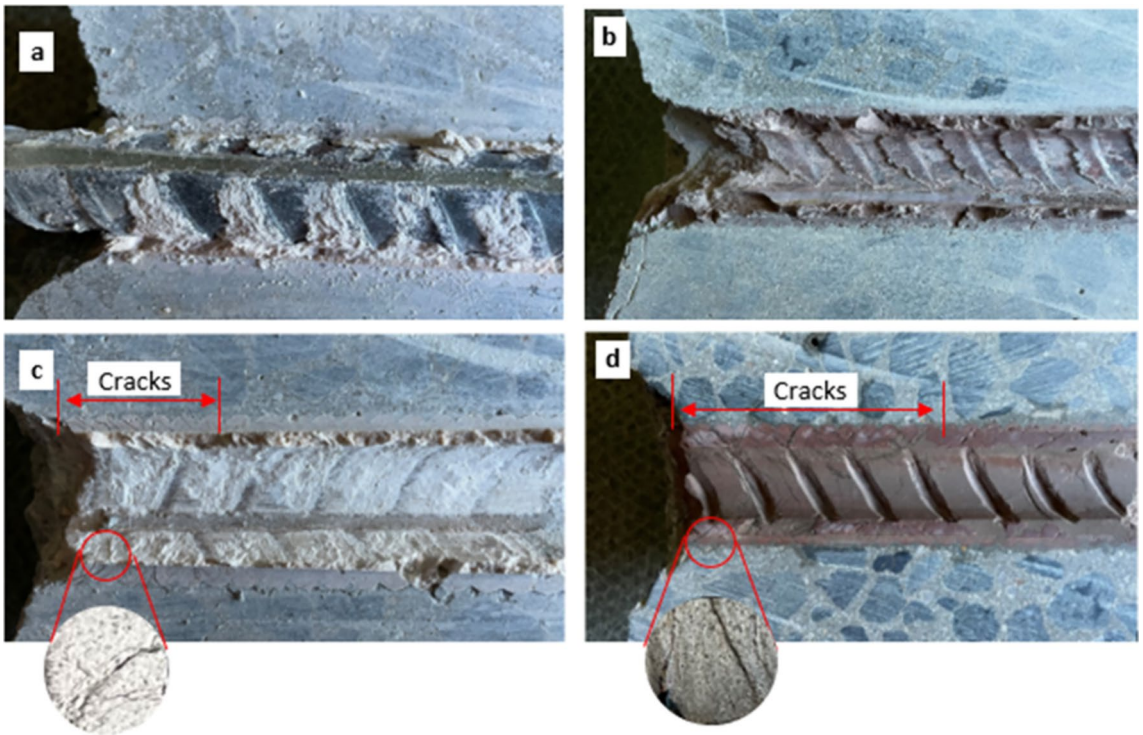

Fig. 17 Failure at the bolt-encapsulation material interface

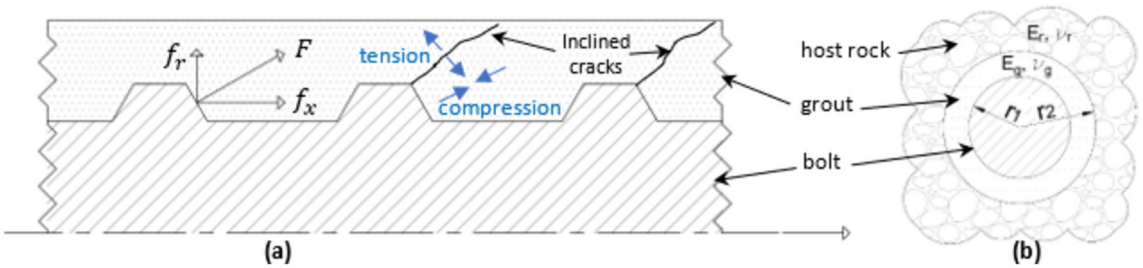

Fig. 18 **a** Exaggerated illustration of the forces subjected at the ribs and the formation inclined cracks, **b** sketch illustrating the parameters used in Eqs. (17) and (18), (adopted from (Zhao et al. 2021))

load applied, and (2) the failure mode. Among all specimens, B3 and A2, which satisfied both conditions, exhibited the greatest degree of damage with cone heights of 35 and 26 mm, respectively. The specimens that failed due to bolt rupture (i.e., A3, A4, and B4) and specimen B1 showed shallow damage, while there was no obvious cone-shaped damage.

In terms of failure at the bolt-bonding material interface, three basic modes of failure were observed: (1) shear-off failure, (2) a combination of hackle cracks and shear-off, and (3) hackle cracks. Shear-off failure was observed in A1, A2, B1, and B2 and occurs due to bolt slip, where irregularities in the bonding materials created by the surface profile of the rock bolt are sheared off and the interface becomes smooth (Fig. 17a, b). This type of failure was the dominant failure mode in cases where the peak pullout load was below the yielding capacity of the bolt. For a direct observation of the state of the specimens after testing, they were longitudinally sliced, and the observation revealed that the bolt-grout surface roughness is distinct depending on the type of encapsulation material. In specimens encapsulated by G1, the grout irregularities are crushed and partially sheared (Fig. 17b, while the bolt-resin surface of specimens encapsulated using resin e.g., R2, were completely sheared and crashed off (Fig. 17a). This may be associated with the mechanical properties of the bonding materials, in particular, the shear strength and the radial stiffness. The radial stiffness provides resistance against the radial deformation induced by the radial component (f_r) of the force acting on the bolt surface, as shown in Fig. 18a. The radial stiffness of the G1 grout obtained from Eq. (17) is over three times that of R2 (Zhao et al. 2021).

$$k_s = E_g\left(r_2^2 - r_1^2\right)/\left[\left(r_2^2 + r_1^2\right) + \left(r_2^2 - r_1^2\right)\nu_g - 2r_2^2\Phi\right], \quad (17)$$

where k_s is the radial stiffness, E_g and ν_g are the elastic modulus and Poisson's ratio of the grout, respectively, r_1 and r_2 are shown in Fig. 18b which are the diameter of the bolt and the hole, respectively, and the factor Φ is expressed as:

$$\Phi = \frac{2r_1^2}{E_g\left(r_2^2 - r_1^2\right)}/\left[\frac{1+\nu_r}{E_r} + \frac{\left(1-\nu_g\right)r_2^2 + \left(1+\nu_g\right)r_1^2}{E_g\left(r_2^2 - r_1^2\right)}\right], \quad (18)$$

where E_r and ν_r are the elastic modulus and Poisson's ratio of the host rock, respectively.

The second type of failure at the bolt-grout interface, which is a combination of circumferential cracks and shear-off failure, was only observed in the B3 specimen, as shown in Fig. 17c. However, circumferential cracks themselves are also visible in the A3, A4, and B4 specimens, as illustrated in Fig. 17d. These cracks are a series of cracks inclined at roughly 45° to the host rock, but they are effectively arrested as they approach the host rock. The circumferential cracks, which are only seen at a distance of 44–65 mm from the surface, can be associated with the level of pullout load and thus the degree of elongation. Once the resultant strain exceeds the elastic capability of the encapsulation media, the cracks begin to form. Apparently, the density of the cracks increases as they approach the loading end, where the strain on the bolt is maximum, leading to extensive damage and thus causing a crush-off zone (Fig. 17d). Therefore, it can be concluded that the inclined cracks in the encapsulating media can only occur in cases where there is considerable

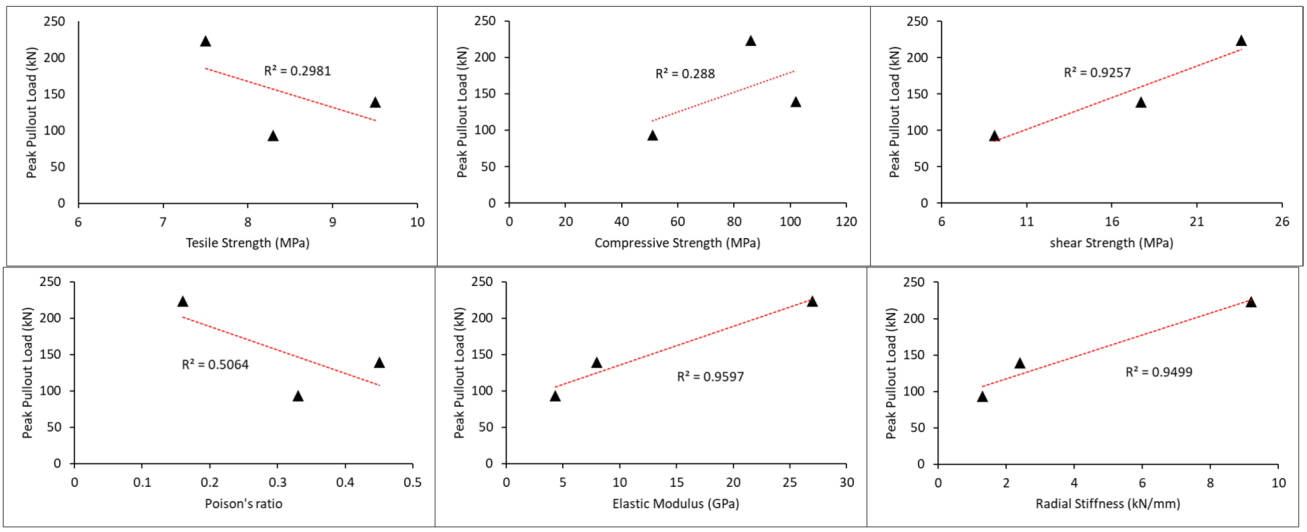

Fig. 19 Correlation between the mechanical characteristics of encapsulation media and the pullout capacity of the system

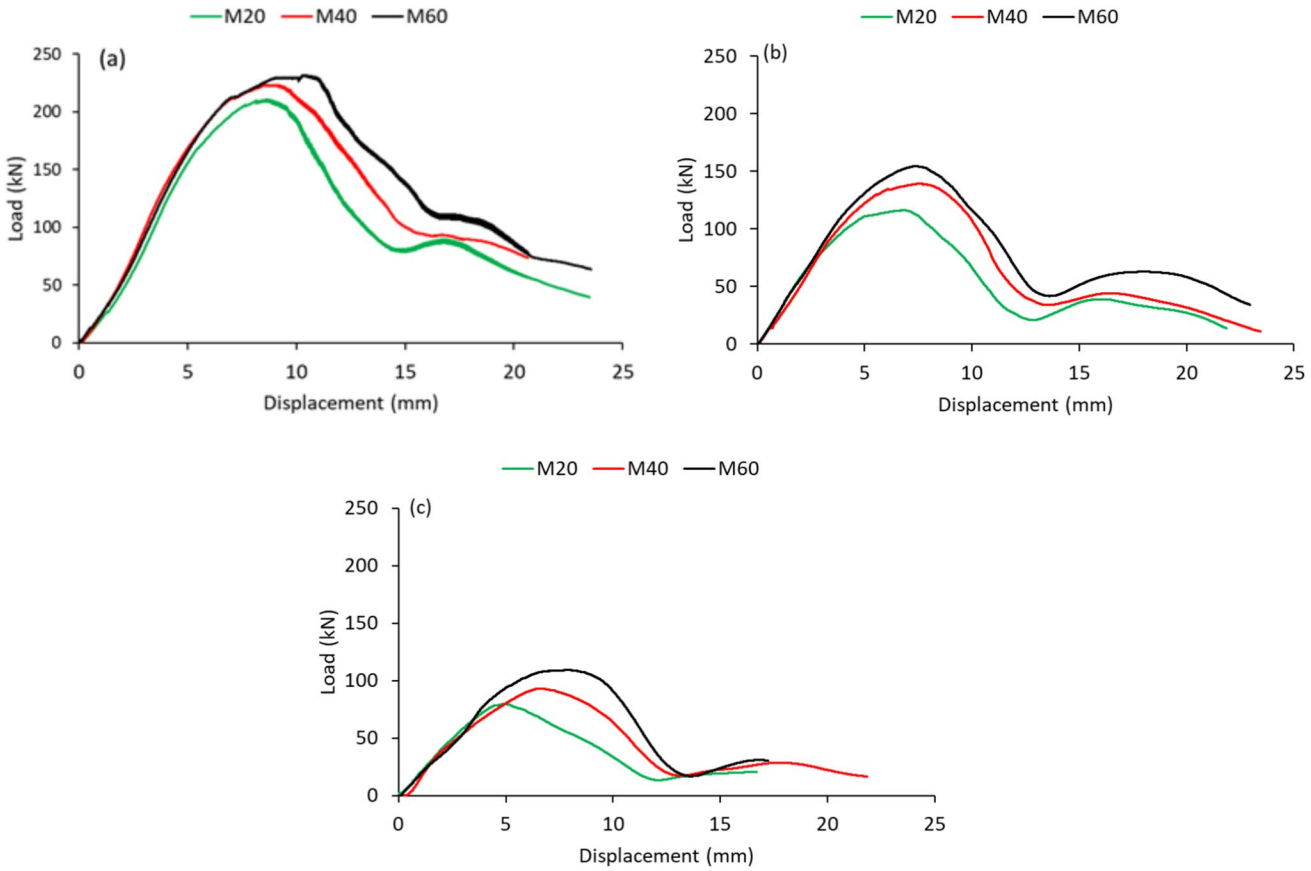

Fig. 20 The effects of the host rock strength and the encapsulation media type on the pullout performance of rock bolts; **a** series C tests, **b** series D tests, and **c** series E tests

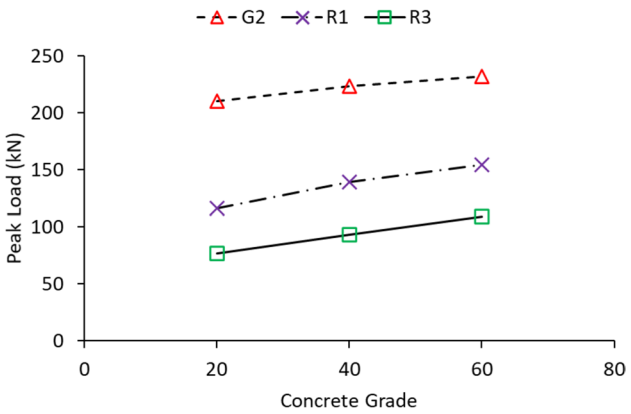

Fig. 21 Peak pullout load vs. host rock strength and the bonding type.

elongation in the bolt (e.g., beyond the yield strength of the bolt) before debonding of the system occurs.

3.3 Effect of Encapsulation Medium and Host Rock on the Pull-Out Performance of Rock Bolts

For further analysis of the effects of bonding material type, as well as the effects of host rock conditions on the axial performance of rock bolts, nine additional pullout tests were conducted on 150 mm bolts encapsulated in three grades of concrete cylinder, including M20, M40, and M60, using three different encapsulation media, including G2, R1, and R3.

Comparing the pullout performance of specimens encapsulated with different media reveals the importance of the mechanical characteristics of the encapsulation media in analyzing the pullout performance of fully encapsulated rock bolts. Key mechanical characteristics, including radial stiffness, tensile strength, and compressive strength, were considered. To analyze the effect of radial stiffness, the elastic modulus and Poisson's ratio were used to calculate

the radial stiffness at the bolt-grout interface using Eq. (17). For simplification, the host rock properties were kept constant, using concrete with a 40 MPa compressive strength. Figure 19 illustrates the effect of these parameters on the pullout performance of rock bolts encapsulated with G1, R1, and R2. The results show a strong correlation between the pullout capacity of the bolts and the shear strength, elastic modulus, and radial stiffness of the grouts.

3.4 Effects of the Bonding Material Type and Host Rock Compressive Strength on Debonding Behavior

Figures 20 presents the load–displacement curves from the pullout tests conducted on specimens encapsulated with G1, R1, and R2, using concrete with compressive strengths of 20, 40, and 60 MPa, and Fig. 21 shows the relation between the peak pullout load and the concrete grades for different bonding materials.

In terms of the effect of the type of bonding material, it was found that at an identical concrete grade (e.g., M20), the highest bearing capacity was represented by the bolt encapsulated using G2 grouting materials, followed by R1, and lastly, R3. The shear and compressive strengths of the bonding agent used in the C series (G1) are lower than that of the D series (54% and 31%); nonetheless, the peak pullout capacity of C1, C2, and C3 is 80%, 60%, and 50% higher than that of D1, D2, and D3, respectively. The reason is rooted in the expansion characteristics of the G2 grout which provided an additional normal force contributing to the shear pullout performance of the rock bolt. For expandable bonding materials, it is commented that when cast in molds for mechanical testing, the bonding agent is free to expand in one direction, while grout injection in the borehole provides higher normal stress resulting in higher bond strength (Benmokrane et al. 2000). Thus, mechanical testing of the expandable materials cast and prepared in conventional molds may result in imprecise results. Amongst all the bonding materials used in this study, specimens bonded using R3, i.e., E1, E2, and E3, exhibited the lowest pullout capacity, as seen in Fig. 20c. This was predicted as R3 also showed lower strength properties compared to the bonding agents.

The results presented in Figs. 20 and 21 demonstrate that the strength of the host rock significantly contributes to the pullout capacity of rock bolts. Axial slip of deformed reinforcing elements generates radial dilation, which is inhibited or restricted by the normal stiffness of the rock mass. A higher radial stiffness may lead to a higher induced lateral confining stress and higher interfacial bond strength (Hyett et al. 1992; Yazici and Kaiser 1992). The peak pullout load of specimens bonded using G2 grout improved from 210.1 to 223.6 kN and then to 231.9 kN as the host rock compressive strength increased from 20 to 40 MPa and then 60 MPa. This indicates an improvement of 6.3% and 3.7%, respectively. Similar improvement in the pullout capacity with an increase in the host rock strength was observed in the other series. In the D series tests, an increase in the host rock compressive strength from 20 to 40 MPa and then 60 MPa caused an improvement in the peak pullout load from 116.1 to 139.2 kN and then to 154.6 kN, respectively. This indicates respective improvements of 19.8% and 11%. Considerable progress can also be observed in the pullout performance of series E with an increase in the concrete compressive strength. In E1, where the bolt was installed in a concrete cylinder with 20 MPa compressive strength, the peak pullout load measured 76.9 kN. This value increased to 93.3 kN and 109.3 kN when the concrete strength increased to 40 MPa and 60 MPa, respectively. This represents an increase of 21.3% and 17.2%, respectively.

4 Conclusion

This study has investigated the mechanical properties of bonding materials and the axial behavior of fully encapsulated rock bolts. The study aimed to understand the effects of embedment length, bonding materials, and host rock conditions on the performance of rock bolts. Mechanical testing was conducted to comprehensively investigate the compressive, tensile, and shear strengths of the bonding materials. Elastic modulus, Poisson's ratio, and shear modulus of the bonding materials were also quantified to analyze the factors affecting the bond stress distribution along the embedment length.

Pullout tests were conducted using deformed steel M24 X Coal Bolts embedded in concrete with three different strength grades. Five types of bonding materials, including two types of cementitious grouts (G1 and G2) and three types of polyester resins (R1, R2, and R3), were used to evaluate the effects of bonding materials on the axial load transfer mechanism of rock bolts. Strain gauges were used to measure the effects of embedment length on the axial performance of rock bolts.

The load–displacement curves for the fully debonded specimens (A1, A2, B1, and B2) exhibited two main trends: an initial linear segment followed by a non-linear one. The linear segment correlated well with the elastic behavior of the steel bolt, indicating that plastic deformation of the bonding system i.e., debonding of the bolt, began when the non-linear behavior commenced. Increasing the embedment length from 100 to 200 mm improved the peak pullout strength by 29–43%. This improvement increased to 62–69% when the embedment length was further increased

to 300 mm. However, once the embedment length exceeded the critical length, the peak pullout load became constant and equal to the tensile strength of the bolt bar. Increasing the embedment length beyond the critical embedment length did not improve the bolting system's performance, as demonstrated by A3 and A4, with 300 mm and 400 mm embedment lengths respectively, which showed a peak pullout capacity of 285 kN. Comparing the results led to the conclusion that the compressive strength of the bonding agent alone cannot predict the pullout performance. For example, the pullout strength of grouted rock bolts using G1 was found to be 10–20% higher than that of bolts encapsulated using the R1 bonding agent, even though G1's compressive strength was 15% less than R1's.

The results obtained from strain gauges showed that the distribution of bond stress depends on the failure mode of the system (i.e., shank rupture and failure at the bolt-grout interface). However, it was found that the level of induced bond stress increases with the increase in pullout load, regardless of the embedment length and distance. The results also revealed that as the embedment length increases, the subjected pullout load diffuses over a longer length, reducing stress concentration. Concerning the mechanical characteristics of the bonding materials, the shear modulus has the most significant impact on the axial load transfer along the encapsulation length and, consequently, on the distribution of induced bond stress at the bolt-grout interface. Based on experimental results and developed mathematical models, it was concluded that an encapsulation material with a lower shear modulus results in a more even distribution of bond stress along the encapsulation length. Conversely, materials with higher shear modulus tend to concentrate bond stress, particularly near the loading end.

In terms of the failure pattern at the bolt-grout interface, three main forms of damage were identified, including shear-off, a combination of shear-off and inclined cracks near the collar, and only inclined cracks without effective debonding. The damage pattern primarily depends on the failure mode of the system and the level of the peak pullout load. Further investigation revealed that the expansion characteristics of the bonding agent are an effective factor in significantly improving the pullout capacity of fully grouted rock bolts. Among all the specimens, series D exhibited the highest bearing capacity values where an expandable grout, G2, was used. Among all the mechanical characteristics of the encapsulation materials, the elastic modulus, radial stiffness, and shear strength were found to have a significant correlation with the pullout capacity of the bolting systems. The results presented in Fig. 20 show that the strength of the host rock also significantly contributes to the pullout capacity of the bolts. It was found that an increase in the compressive strength of the concrete from 20 to 60 MPa resulted in an increase of approximately 3–20% in the pullout strength of the bolt.

The findings of this study significantly advance both the theoretical understanding and practical applications of rock bolt systems. The identification of critical mechanical properties, such as elastic modulus, radial stiffness, and shear strength, provides a theoretical framework for optimizing bonding materials. This information is crucial for the effective design and enhancement of reinforcing systems. Practically, the insights into the effects of embedment length, bonding materials, and host rock strength on pullout performance can inform the development and implementation of more efficient rock bolting systems, leading to improved stability and safety in rock engineering applications.

5 Limitation of the Study

The study results highlight the influence of parameters such as encapsulation length, grout type, and host rock on the behavior of fully grouted rock bolts. However, practical limitations should be acknowledged and studied in depth. Further research is recommended to explore the effects of different configurations, particularly investigating the impact of bolt pre-tensioning on the axial performance of fully grouted rock bolts.

Funding Open Access funding enabled and organized by CAUL and its Member Institutions.

Data availability The data supporting the findings of this study are available upon request from the corresponding author.

Declarations

Conflict of interest The authors declare that they have no conflict of interest.

References

Antino TD, Sneed LH, Carloni C, Pellegrino C (2016) Effect of the inherent eccentricity in single-lap direct-shear tests of PBO

FRCM-concrete joints. Compos Struct 142:117–129. https://doi.org/10.1016/j.compstruct.2016.01.076
AS 1379 (1997) Specification and supply of concrete. Aust. Stand
ASTM C192 (2015) Standard practice for making and curing concrete test specimens in the Laboratory. ASTM Int. https://doi.org/10.1520/C0192_C0192M-14
ASTM C109 (2020) Standard Test Method for Compressive Strength of Hydraulic Cement Mortars (Using 2-in. or [50 mm] Cube Specimens). ASTM Int. https://doi.org/10.1520/C0109_C0109M-20
ASTM C39 (2021) Standard test method for compressive strength of cylindrical concrete specimens. ASTM Int. https://doi.org/10.1520/C0039_C0039M-21
ASTM C469 (2021) Standard test method for static modulus of elasticity and poisson's ratio of concrete in compression. ASTM Int. https://doi.org/10.1520/C0469_C0469M-14
ASTM C307 (2023) Standard test method for tensile strength of chemical-resistant mortar, grouts, and monolithic surfacings. ASTM Int. https://doi.org/10.1520/C0307-18
ASTM C579 (2023) Standard test methods for compressive strength of chemical-resistant mortars, grouts, monolithic surfacings, and polymer concretes. ASTM Int. https://doi.org/10.1520/C0579-18
ASTM D5379 (2021) Standard test method for shear properties of composite materials by the V-notched beam method. ASTM Int. https://doi.org/10.1520/D5379_D5379M-19E01
ASTM D638 (2022) standard test method for tensile properties of plastics. ASTM Int. https://doi.org/10.1520/D0638-14
Aziz N, Craig P, Mirzaghorbanali A, Nemcik J (2016) Factors influencing the quality of encapsulation in rock bolting. Rock Mech Rock Eng 49:3189–3203. https://doi.org/10.1007/s00603-016-0973-5
Benge M, Katende A, Rutqvist J, Radonjic M, Bunger A (2023) Creep properties of shale and predicted impact on proppant embedment for the caney shale. Oklahoma Rock Mech Rock Eng 56:5903–5921. https://doi.org/10.1007/s00603-023-03362-8
Benge M, Lu Y, Katende A, Rutqvist J, Crandall D, Haecker A, King G, Renk JB, Radonjic M, Bunger A (2021) Connecting geomechanical properties with potential for proppant embedment and production decline for the emerging Caney Shale, Oklahoma. SPE/AAPG/SEG Unconv. Resour. Technol. Conf. https://doi.org/10.15530/urtec-2021-5084
Benmokrane B, Chennouf A, Mitri HS (1995) Laboratory evaluation of cement-based grouts and grouted rock anchors. Int J Rock Mech Min Sci Geomech Abstr 32:633–642
Benmokrane B, Zhang B, Chennouf A (2000) Tensile properties and pullout behaviour of AFRP and CFRP rods for grouted anchor applications. Constr Build Mater 14:157–170
Cai Y, Esaki T, Jiang Y (2004) An analytical model to predict axial load in grouted rock bolt for soft rock tunnelling. Tunn Undergr Sp Technol 19:607–618. https://doi.org/10.1016/j.tust.2004.02.129
Cao C, Ren T, Cook C, Cao Y (2014) Analytical approach in optimising selection of rebar bolts in preventing rock bolting failure. Int J Rock Mech Min Sci 72:16–25. https://doi.org/10.1016/j.ijrmms.2014.04.026
Cao C, Ren T, Zhang Y, Zhang L, Wang F (2016) Experimental investigation of the effect of grout with additive in improving ground support. Int J Rock Mech Min Sci 85:52–59. https://doi.org/10.1016/j.ijrmms.2015.12.010
Chen J, Li D (2022) Numerical simulation of fully encapsulated rock bolts with a tri-linear constitutive relation. Tunn Undergr Sp Technol 120:104265. https://doi.org/10.1016/j.tust.2021.104265
Chen Y, Xiao H (2024) State-of-the-art on the anchorage performance of rock bolts subjected to shear load. Int J Coal Sci Technol. https://doi.org/10.1007/s40789-023-00643-z
Chen J, He F, Zhang S (2020) A study of the load transfer behavior of fully grouted rock bolts with analytical modelling. Int J Min Sci Technol 30:105–109. https://doi.org/10.1016/j.ijmst.2019.12.010
Farmer IW (1975) Stress distribution along a resin-grouted rock anchor. Int J Rock Mech Min Sci Geomech Abstr 12:347–351
Freeman TJ (1978) Behaviour of fully bonded rock bolts in the kielder experimental tunnel. Int J Rock Mech Min Sci Geomech Abstr 15:37–40. https://doi.org/10.1016/0148-9062(78)91073-2
Grasselli G (2005) 3D Behaviour of bolted rock joints: experimental and numerical study. Int J Rock Mech Min Sci 42:13–24. https://doi.org/10.1016/j.ijrmms.2004.06.003
He L, An X, Zhao Z (2015) Fully grouted rock bolts: an analytical investigation. Rock Mech Rock Eng. https://doi.org/10.1007/s00603-014-0610-0
Høien AH, Li CC, Zhang N (2021) Pull-out and critical embedment length of grouted rebar rock bolts-mechanisms when approaching and reaching the ultimate load. Rock Mech Rock Eng 54:1431–1447. https://doi.org/10.1007/s00603-020-02318-6
Huang M, Zhou Z, Huang Y, Ou J (2013) A distributed self-sensing FRP anchor rod with built-in optical fiber sensor. Measurement 46:1363–1370. https://doi.org/10.1016/j.measurement.2012.12.012
Hyett AJ, Bawden WF, Reichert RD (1992) The effect of rock mass confinement on the bond strength of fully grouted cable bolts. Int Rock Mech Min Sci Geomech Abstr 29:503–524
Katende A (2022) The impact of rock lithology and microstructural properties on proppant embedment and fracture conductivity: a case study of the Caney Shale, Southern Oklahoma, USA. ProQuest Diss. Theses. Oklahoma State University PP—United States—Oklahoma, United States—Oklahoma
Katende A, Lu Y, Bunger A, Radonjic M (2020) Experimental quantification of the effect of oil based drilling fluid contamination on properties of wellbore cement. J Nat Gas Sci Eng 79:103328. https://doi.org/10.1016/j.jngse.2020.103328
Katende A, Rutqvist J, Benge M, Seyedolali A, Bunger A, Puckette JO, Rhin A, Radonjic M (2021) Convergence of micro-geochemistry and micro-geomechanics towards understanding proppant shale rock interaction: a Caney shale case study in southern Oklahoma, USA. J Nat Gas Sci Eng 96:104296. https://doi.org/10.1016/j.jngse.2021.104296
Katende A, Allen C, Massion C, Awejori AG, Xiong F, Radonjic M, Rutqvist J, Nakagawa S (2022) Experiments and modeling of proppant embedment and fracture conductivity for the Caney Shale, Oklahoma, USA. 56th U.S. Rock Mech. Symp. https://doi.org/10.56952/ARMA-2022-0805
Katende A, Rutqvist J, Massion C, Radonjic M (2023) Experimental flow-through a single fracture with monolayer proppant at reservoir conditions: a case study on Caney Shale, Southwest Oklahoma, USA. Energy 273:127181. https://doi.org/10.1016/j.energy.2023.127181
Li C, Stillborg B (2000) Analytical models for rock bolts. Int J Rock Mech Min Sci 36:1013–1029
Li CC, Kristjansson G, Høien AH (2016) Critical embedment length and bond strength of fully encapsulated rebar rockbolts. Tunn Undergr Sp Technol 59:16–23. https://doi.org/10.1016/j.tust.2016.06.007
Li D, Li Y, Chen J, Masoumi H (2021) An analytical model for axial performance of rock bolts under constant confining pressure based on continuously yielding criterion. Tunn Undergr Sp Technol Inc Trenchless Technol Res 113:103955. https://doi.org/10.1016/j.tust.2021.103955
Ma S, Nemcik J, Aziz N (2013) An analytical model of fully grouted rock bolts subjected to tensile load. Constr Build Mater 49:519–526. https://doi.org/10.1016/j.conbuildmat.2013.08.084
Małkowski P, Feng X, Niedbalski Z, Żelichowski M (2022) Laboratorial tests and numerical modeling of rock bolts bonded by different materials. Rock Mech Rock Eng. https://doi.org/10.1007/s00603-022-03191-1

Martín LB, Tijani M, Hadj-hassen F (2011) A new analytical solution to the mechanical behaviour of fully grouted rockbolts subjected to pull-out tests. Constr Build Mater 25:749–755. https://doi.org/10.1016/j.conbuildmat.2010.07.011

McKay KS, Erki MA (1993) Grouted anchorages for aramid fibre reinforced plastic prestressing tendons. Can J Civ Eng 20:1065–1069. https://doi.org/10.1139/l93-137

Moosavi M, Jafari A, Khosravi A (2005) Bond of cement grouted reinforcing bars under constant radial pressure. Cem Concr Compos 27:103–109. https://doi.org/10.1016/j.cemconcomp.2003.12.002

Nourizadeh H, Williams S, Mirzaghorbanali A, McDougall K, Aziz N, Serati M (2021) Axial behaviour of rock bolts-part (A) Experimental study. In: Resource operator conference. Springfield, Queensland, pp 294–302

Nourizadeh H, Mirzaghorbanali A, Mcdougall K, Jeewantha LHJ, Craig P, Motallebiyan A, Jodeiri B, Rastegarmanesh A, Aziz N (2023a) Characterization of mechanical and bonding properties of anchoring resins under elevated temperature. Int J Rock Mech Min Sci 170:105506. https://doi.org/10.1016/j.ijrmms.2023.105506

Nourizadeh H, Mirzaghorbanali A, Serati M, Mahmoud M-A, McDougall K, Aziz N (2023b) Failure characterization of fully grouted rock bolts under triaxial testing. J Rock Mech Geotech Eng. https://doi.org/10.1016/j.jrmge.2023.08.013

Rastegarmanesh A, Mirzaghorbanali A, McDougall K, Aziz N, Anzanpour S, Nourizadeh H, Moosavi M (2022) Axial performance of cementitious grouted cable bolts under rotation constraint scenarios. Rock Mech Rock Eng. https://doi.org/10.1007/s00603-022-02950-4

Rastegarmanesh A, Mirzaghorbanali A, McDougall K, Aziz N, Anzanpour S, Nourizadeh H, Moosavi M (2023) Axial response of resin encapsulated cable bolts in monotonic and cyclic loading. Can Geotech J. https://doi.org/10.1139/cgj-2022-0379

Ren FF, Yang ZJ, Chen JF, Chen WW (2010) An analytical analysis of the full-range behaviour of grouted rockbolts based on a tri-linear bond-slip model. Constr Build Mater 24:361–370. https://doi.org/10.1016/j.conbuildmat.2009.08.021

Signer SP (1990) Field verification of load transfer mechanics of fully grouted roof bolts, 9301. United States. Bureau of Mines

Singer SP, Cox D, Johnston J (1997) A method for the selection of rock support based on bolt loading measurements, Spokane Research Center, NIOSH

Sun H, Liu H, Liu X, Ye Z (2024) Mechanical testing and numerical simulation of intelligent terminal structure of rockbolt used as a deformable support and for safety monitoring in rock engineering. Tunn Undergr Sp Technol 148:105769. https://doi.org/10.1016/j.tust.2024.105769

Tepfers R (1979) Cracking of concrete cover along anchored deformed reinforcing bars. Mag Concr Res 31:3–12

Teymen A, Kılıç A (2018) Effect of grout strength on the stress distribution (tensile) of fully-grouted rockbolts. Tunn Undergr Sp Technol 77:280–287. https://doi.org/10.1016/j.tust.2018.04.022

Vlachopoulos N, Cruz D, Forbes B (2018) Utilizing a novel fiber optic technology to capture the axial responses of fully grouted rock bolts. J Rock Mech Geotech Eng 10:222–235. https://doi.org/10.1016/j.jrmge.2017.11.007

Wee S, Kang S, Hai K, Yang E (2016) Experimental and analytical investigation on bond-slip behaviour of deformed bars embedded in engineered cementitious composites. Constr Build Mater 127:494–503. https://doi.org/10.1016/j.conbuildmat.2016.10.036

Wu Y, Hao Y, Tao J, Teng Y, Dong X (2019) Non-destructive testing on anchorage quality of hollow grouted rock bolt for application in tunneling, lessons learned from their uses in coal mines. Tunn Undergr Sp Technol. https://doi.org/10.1016/j.tust.2019.103094

Wu T, Huang F, Zhang D, An Y (2024) Anchorage failure mechanism and uplift bearing capacity of L- & J-anchor bolts in plain concrete. Eng Fail Anal. https://doi.org/10.1016/j.engfailanal.2024.107991

Yang S, Wu Z, Hu X, Zheng J (2008) Theoretical analysis on pullout of anchor from anchor–mortar–concrete anchorage system. Eng Fract Mech 75:961–985. https://doi.org/10.1016/j.engfracmech.2007.05.004

Yazici S, Kaiser PK (1992) Bond strength of grouted cable bolts. Int J Rock Mech Min Sci Geomech Abstr 29:279–292

Yilmaz S, Özen MA, Yardim Y (2013) Tensile behavior of post-installed chemical anchors embedded to low strength concrete. Constr Build Mater 47:861–866. https://doi.org/10.1016/j.conbuildmat.2013.05.032

Yokota Y, Zhao Z, Nie W, Date K, Iwano K, Okada Y (2019) Experimental and numerical study on the interface behaviour between the rock bolt and bond material. Rock Mech Rock Eng 52:869–879. https://doi.org/10.1007/s00603-018-1629-4

Zhang B, Benmorkane B, Ebead UAA (2006) Design and evaluation of fiber-reinforced polymer bond-type anchorages and ground anchors. Int J Geomech 166

Zhao T, Zhang Y, Li CC (2021) Radial stiffness of rock bolt samples and required thickness of the steel tube in impact tests. Int J Rock Mech Min Sci 146:104886. https://doi.org/10.1016/j.ijrmms.2021.104886

Zhou Y-W, Wu Y-F, Yun Y (2010) Analytical modeling of the bond–slip relationship at FRP-concrete interfaces for adhesively-bonded joints. Compos Part B Eng 41:423–433. https://doi.org/10.1016/j.compositesb.2010.06.004

Zou X, Sneed LH, D'Antino T (2020) Full-range behavior of fiber reinforced cementitious matrix (FRCM)-concrete joints using a trilinear bond-slip relationship. Compos Struct. https://doi.org/10.1016/j.compstruct.2020.112024